MULTISCALAR LINE MEASUREMENTS IN NONISOBARIC HIGH-PRESSURE UNDEREXPANDED SUPERSONIC JETS USING ROTATIONAL-VIBRATIONAL RAMAN SPECTROSCOPY

A Thesis

by

BENJAMIN NATHAN COHEN

Submitted to the Office of Graduate Studies of
Texas A&M University
in partial fulfillment of the requirements for the degree of

MASTER OF SCIENCE

May 2008

Major Subject: Aerospace Engineering

MULTISCALAR LINE MEASUREMENTS IN NONISOBARIC HIGH-PRESSURE UNDEREXPANDED SUPERSONIC JETS USING ROTATIONAL-VIBRATIONAL RAMAN SPECTROSCOPY

A Thesis

by

BENJAMIN NATHAN COHEN

Submitted to the Office of Graduate Studies of
Texas A&M University
in partial fulfillment of the requirements for the degree of

MASTER OF SCIENCE

Approved by:

Chair of Committee,	Adonios N. Karpetis
Committee Members,	Othon K. Rediniotis
	Kalyan Annamalai
Head of Department,	Helen Reed

May 2008

Major Subject: Aerospace Engineering

ABSTRACT

Multiscalar Line Measurements in Nonisobaric High-pressure Underexpanded

Supersonic Jets Using Rotational-Vibrational Raman Spectroscopy. (May 2008)

Benjamin Nathan Cohen, B.S., University of Oklahoma

Chair of Advisory Committee: Dr. Adonios N. Karpetis

This work describes the development of a Raman spectroscopy system for measuring aerothermochemistry in high-speed jets and flames. A transmissive grating spectrometer was newly developed for capturing pure rotational Raman and rotational-vibrational Raman with a single CCD camera. Previous state-of-the-art experiments applied line imagining in known flowfields of constant pressure. The system described herein is designed to provide local measurement of pressure, with full thermochemistry, along a line. In every point, temperature will be measured by examining the Boltzmann decay of the rotational spectrum, while molar fraction will be measured from the vibrational Raman spectrum. The temperature and concentrations will then be combined to obtain partial pressure measurements via the equation of state. This work examines the phenomenology of rotational and vibrational Raman scattering and proposes algorithms that can be used for data extraction.

ACKNOWLEDGEMENTS

TABLE OF CONTENTS

LIST OF FIGURES

Page

LIST OF TABLES

1. INTRODUCTION

1.1   General

The motivation behind this research is to investigate the process of combustion in supersonic environments. The combustion process is the conversion of chemical energy into thermal energy; however it involves finite time scales[1]. Therefore, producing combustion in a high-speed environment introduces troublesome issues. Extinction, when the flame is blown out, is a significant problem. Combustion must be accomplished within millisecond timescales by the supersonic flows that exist within scramjet engines[2]. Experiments with functioning scramjet engines have been performed by NASA, but have generally been short in duration. An early powered free flight test of NASA's X-43[3] lasted approximately 10s.

Experimental methods for characterizing flows are well established. Velocity and temperature of a gas mixture can readily be measured with a pitot probe[4] and thermocouple[5], respectively. These instruments are often used for diagnostics in wind tunnels, where the size of the probes may be insignificant compared to the tunnel test section. The problem with probes is that they are intrusive in nature and thus disturb the flow[6]. This is rather problematic in combustion where the probes not only interfere with the flow, thus changing the results and the flame itself, but may not be able to sustain the high temperatures seen in combustion.

_____

This thesis follows the style of the *AIAA Journal.*

Laser diagnostics, however, can extract data and information from a flow by making in-situ, non-intrusive measurements. This ability has made laser diagnostics a preferred diagnostic tool for characterizing combustion and has inspired a considerable research effort throughout the scientific community[7].

Two prominent methods for using laser diagnostics in combustion are Raman and Rayleigh scattering techniques[8]. Rayleigh scattering can provide useful information on a gas mixture, but is not species specific. Raman scattering, on the other hand, is species specific, but suffers from low signal levels that are approximately three orders of magnitude less than Rayleigh scattering for the vibrational spectrum[8].

1.2   *Objective*

The objective of this research is to develop a Raman spectroscopy system capable of characterizing the aerothermochemistry (pressure, temperature, and molar fractions) of jet flames. This system utilizes both pure rotational and rotational-vibrational spontaneous Raman scattering to obtain the desired measurements. This is performed using one camera as part of a single Raman spectrometer developed in the laboratory.

The intended application of this system is to examine the aerothermochemistry of nonisobaric, underexpanded, supersonic jets at high pressures using multiscalar line imagining. These flow conditions are analogous to a scramjet engine and are therefore of interest to the aerospace propulsion field. A jet of the aforementioned conditions serves as a canonical model of a scramjet engine. It is necessary to create models of this

type due to the difficulty of gaining laser access in an actual scramjet or other engine. Introducing windows to such machinery for optical access is rather difficult. Algorithms for measuring temperature from the pure rotational Raman spectrum and pressure and species concentrations from the rotational-vibrational Raman spectrum are presented.

1.3   *Previous Work*

Previous combustion research using spectroscopy to measure aerothermochemistry has been performed employing a combination of Raman and Rayleigh scattering for point measurements in jet flames[9]. Rayleigh scattering is rather limited, due to its elastic nature and thus the inability to distinguish individual species, to simple systems (i.e. binary) with flow restrictions (i.e. isobaric and/or isothermal, possibly non-reacting) and often requires some flow properties to be known *a priori*[10]. The Raman/Rayleigh combination has also been successfully used for line imaging of turbulent flames[11, 12]. To employ Rayleigh and Raman scattering simultaneously at least two cameras are needed. This is due to the fact that the Rayleigh signal is roughly three orders of magnitude larger than the vibrational Q-branch Raman signal[13]. The CCD becomes saturated when collecting both Rayleigh and Raman scattering on a single CCD.A lack of resolution for Raman techniques, due to the dynamic range of the CCD, may also hinder this method. Using two cameras is certainly a viable way to take state measurements, however it is more complicated and expensive since additional equipment and setup is necessary along with the task of timing and aligning the cameras with one another to assure correct shot-to-shot data alignment. Using one camera

eliminates this complexity, but requires the Rayleigh signal to be filtered out, forcing the use of Raman scattering for all measurements.

Measurements via the Stokes/anti-Stokes ratio method have been performed by many investigators in the past, *e.g.* Wehrmeyer *et. al.*[14]. The temperature is a function of rotational quantum number (J) and the measured intensities at an initial rotational state (J') and a final state (J). A relationship for the Stokes rotational temperature measurement is shown in Equation (1)[15].

$$T_{S,ro} = \frac{[J'(J'+1) - J(J+1)]\frac{hcB}{k}}{ln\left\{\left(\frac{I_J}{I_{J'}}\right)\left[\frac{\frac{(J'+1)(J'+2)}{2J+3}}{\frac{(J+1)(J+2)}{2J+3}}\right]\left(\frac{v_o - 4B\left(J' + \frac{3}{2}\right)}{v_o - 4B\left(J + \frac{3}{2}\right)}\right)^4\right\}} \quad (1)$$

In Equation (1) h is Planck's constant, c is the speed of light, B is the rotational constant, k is the Boltzmann constant, I_J is the intensity of the subsequent rotational state, $I_{J'}$ is the intensity of the initial rotational state, and v_o is the excitation wavenumber. The rotational quantum number can be determined by from the spectrum with adequate resolution. A major problem associated with this approach is the extremely weak anti-Stokes signal at lower temperatures[14].

2. THEORY

2.1 Rotational Raman

2.1.1   Rotational Raman Profiles

The theoretical rotational profiles are found by calculating the energy levels over a range of the rotational quantum number (J). The reduced mass (μ) of the scattering species, primarily nitrogen and oxygen for air, affects the rotational energy levels. For diatomic molecules μ is calculated by Equation (2)[16]:

$$\mu = \frac{M_1 M_2}{M_1 + M_2} \tag{2}$$

where M_1 and M_2 are the atomic masses of the elements that form the molecule. For homonuclear diatomic molecules, such as N_2 and O_2, $M_1 = M_2$. The reduced mass is then multiplied by the square of the atomic bond length (r) to obtain the molecule's moment of inertia (I) as seen in Equation (3)[15].

$$I = \mu r^2 \tag{3}$$

The moment of inertia is needed to calculate the rotational constant, B, which differs for each species and influences the rotational energy level spacing. Species with larger

values for B will have more compact energy levels than species with smaller B values. B is defined by Equation (4)[15], where h is Planck's constant and c is the speed of light.

$$B = \frac{h}{8\pi^2 cI} \tag{4}$$

The rotational energy, F(J), of a linear diatomic molecule is a function of the rotational quantum number and is calculated by Equation (5)[13] using the rigid rotor approximation.

$$F(J) = BJ(J + 1) \tag{5}$$

Note that F(J) is calculated in units of inverse centimeters, therefore careful attention must be paid to converting the length components of B appropriately. Equation (5) calculates the energy of one rotational level, so the rotational population distribution must be found in order to create the entire profile. Equation (6)[13] calculates the number, N_J, of scatterers in each rotational energy level as a function of J and temperature (T):

$$N_J = \frac{N}{Q_{rot}} g_I (2J + 1) e^{-BJ(J+1)\frac{hc}{kT}} \tag{6}$$

$$Q_{rot} = \frac{kT}{hcB} \tag{7}$$

where N is the number density, Q_{rot} is the partition function for the quantization of rotational energy and is shown in Equation (7)[13], g_I is the nuclear spin degeneracy, and k is the Boltzmann constant.

Rotational profiles are generated by this method over a range of temperatures. It is seen that as temperature increases the peak of the profile decreases and shifts to higher rotational levels while the rate of decay is reduced. Convolving the rotational lines for nitrogen and oxygen it is apparent that oxygen is roughly one third the intensity of nitrogen at the same temperature. This is expected given that air is approximately 79% nitrogen. The intensity of oxygen compared to that of nitrogen is greater than the gas's composition would suggest due to the fact that oxygen, being a heavier molecule (atomic mass of 32 compared to 28), has a greater scattering cross section. Equation (8) shows how the rotational scattered intensity in air depends on the scattering cross sections and molar fractions of the gas mixture's constituents.

$$I_{air} \sim X_{N_2} \left(\frac{\partial \sigma}{\partial \Omega} \right)_{N_2,rot} + X_{O_2} \left(\frac{\partial \sigma}{\partial \Omega} \right)_{O_2,rot} \tag{8}$$

If the two gases were in equal proportion the oxygen lines would be more intense than the nitrogen lines. Figure 1 shows the profile for nitrogen at 300K in terms of the rotational constant.
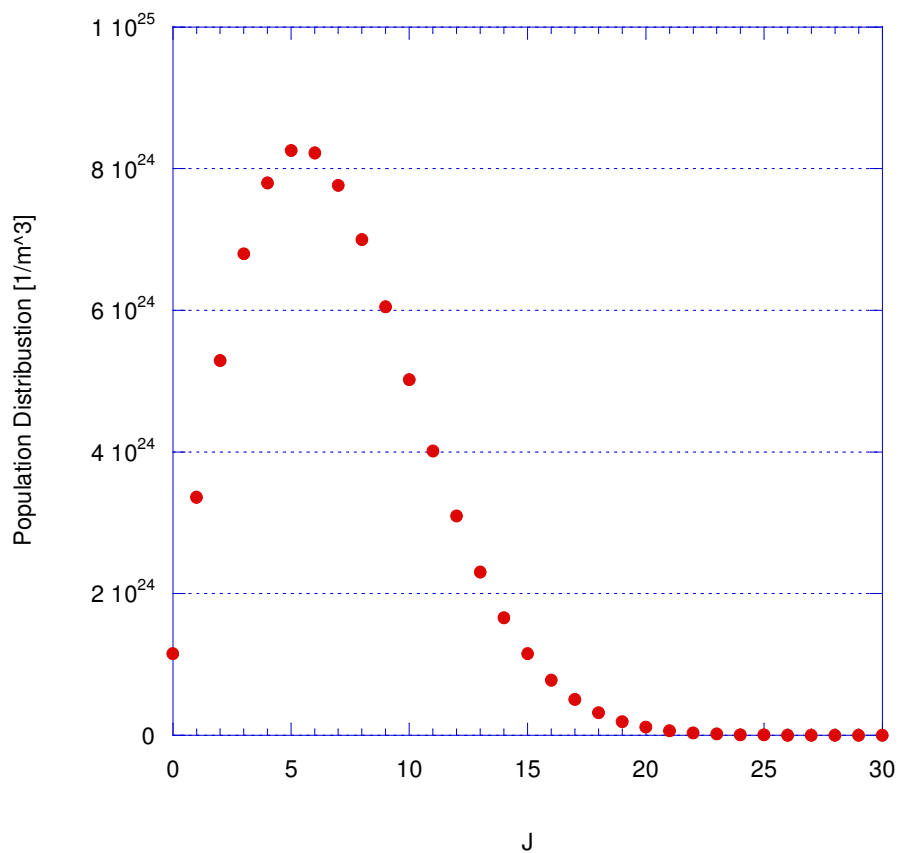
Fig. 1 Rotational Profile of Nitrogen at 300K

2.1.2   Rotational Raman Spectroscopy

The pure rotational spectrum, given a high resolution collection system and ignoring line broadening, would appear as a series of delta functions. Figure 2 shows a theoretical spectrum of air (79% nitrogen, 21% oxygen) that was calculated for 300 K.
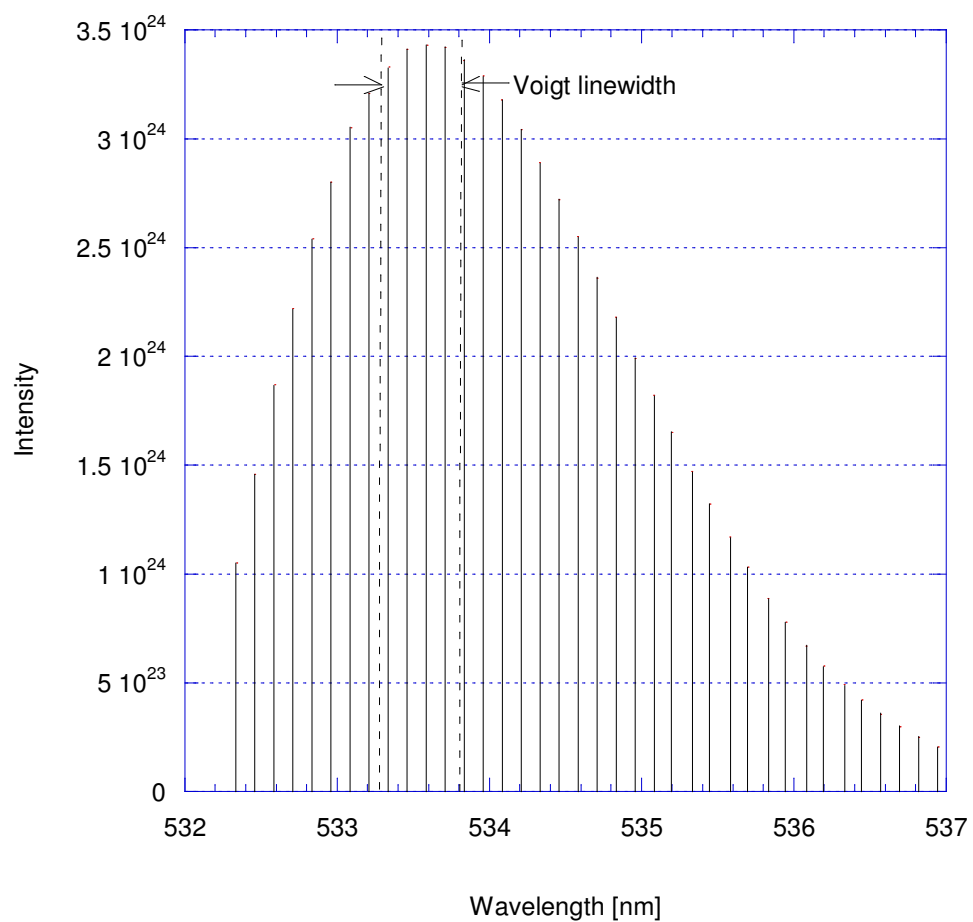
Fig. 2 Rotational Stokes Intensity of Nitrogen and Oxygen at 300K

Each delta function in the graph is the intensity for a different J.   In reality, line broadening effects contribute a width to each delta function to the point where they overlap and form a smooth profile.

The line width, or width of the delta functions, is predicted by the Voigt profile, which is appropriate when both Gaussian (temperature) and Lorentzian (pressure)

broadening significantly contribute to the line width. This usually occurs at higher pressures[17]. The Voigt profile is a convolution of Gaussian and Lorentzian broadening and its parameters, a and x, are defined by Equations (9)[18] and (10)[18].

$$a = (ln2)^{.5} \frac{\Delta v_c}{\Delta v_D} \qquad (9)$$

$$x = 2(ln2)^{.5} \frac{v - v_c}{\Delta v_D} \qquad (10)$$

In these parameters Δv_c is the full width of the collision broadening[18], Δv_D is the full width at half max (FWHM)[13], v is the frequency, and v_c is the central frequency of the profile[13]. The Voigt profile is then the integral shown in Equation (11)[13].

$$V(a, x) = \frac{a}{\pi} \int_{-\infty}^{\infty} \frac{e^{-y^2}}{a^2 + (x - y)^2} dy \qquad (11)$$

The lineshape function is then expressed by Equation (12)[13].

$$g(v) = 2 \left(\frac{ln2}{\pi}\right)^{.5} \frac{V(a, x)}{\Delta v_D} \qquad (12)$$

It is possible to use the Boltzmann decay of the rotational Raman spectrum to extract a temperature measurement. To do this experimental data is compared to

theoretical data. The theoretical data, as generated in the previous section, must be converted in to the same form as the experimental data in order to do a comparison. First, the profiles for nitrogen and oxygen are constructed. These two profiles must be convolved to obtain one profile. Due to the different properties of the nitrogen and oxygen molecules, the two species have different spacing between rotational energy levels. This can be seen in easily in wavelength space. The conversion of profiles to wavelength space is necessitated by the fact that the experimental data is seen in wavelength space rather than J space. Equations $(13)^{13}$ and (14) transform the J values into wavelengths:

$$\bar{\nu}_{Srot} = \bar{\nu}_o - 4B\left(J + \frac{3}{2}\right) \qquad (13)$$

$$\lambda_S = (\bar{\nu}_{Srot})^{-1} \qquad (14)$$

where $\bar{\nu}_{Srot}$ is the Stokes rotational wavenumber, $\bar{\nu}_o$ is the incident wavenumber (1/532nm), and λ_S is the Stokes wavelength.

Figure 3 plots the rotational profiles for oxygen and nitrogen at 300K. It is clear that the two species have rather different energy level spacing as seen in the spacing between data points (corresponding to the peak of each level); nitrogen's energy levels are spaced much further apart than oxygen's.
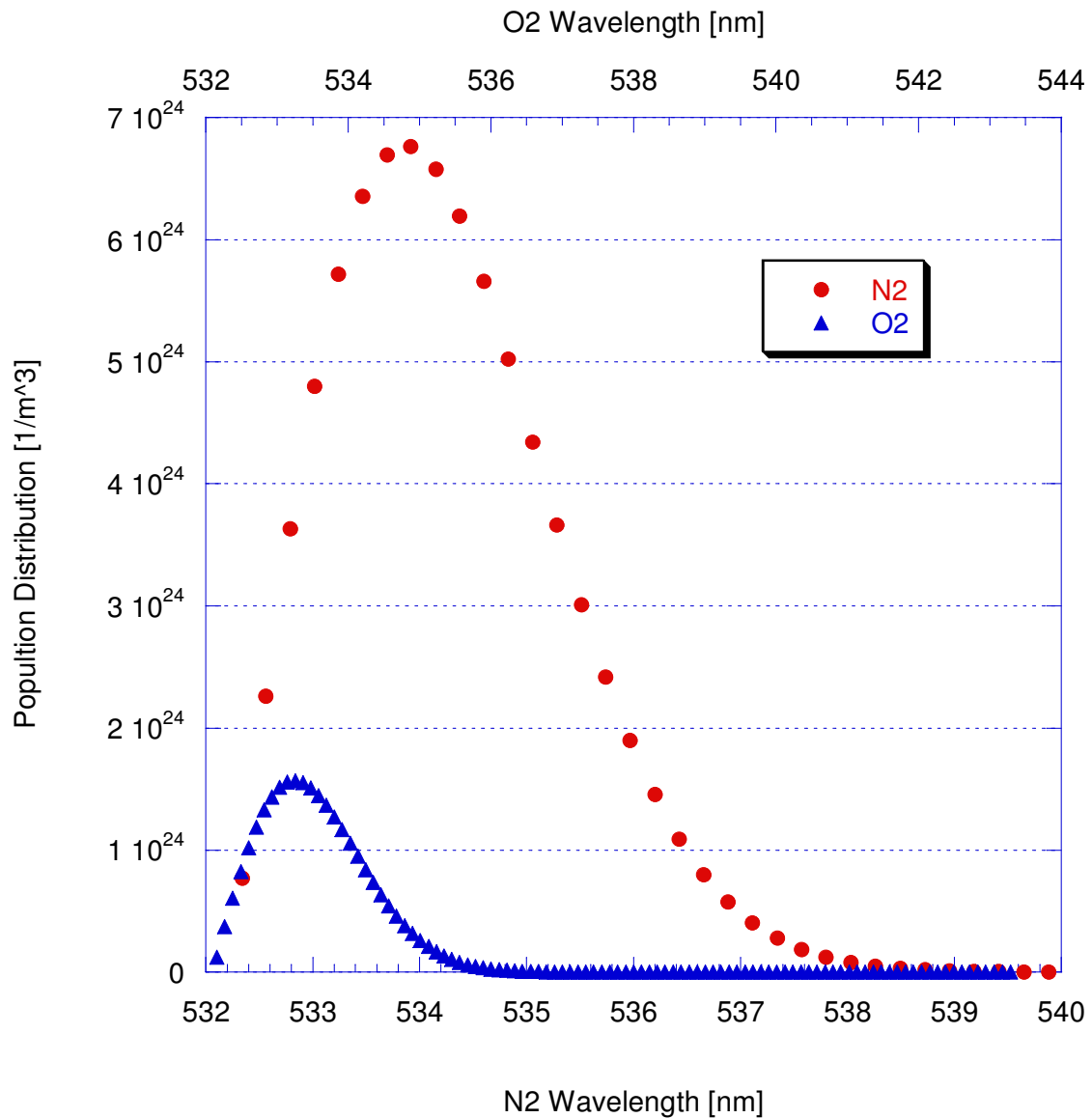
Fig. 3 Rotational Stokes Profiles of Nitrogen and Oxygen at 300K

In order to combine these profiles the oxygen profile is interpolated at the wavelengths of nitrogen. This returns the values of the oxygen profile at wavelengths corresponding to the energy levels of nitrogen, as seen in Fig. 4. Combining the oxygen and nitrogen profiles result in a single profile as seen in Fig. 5.
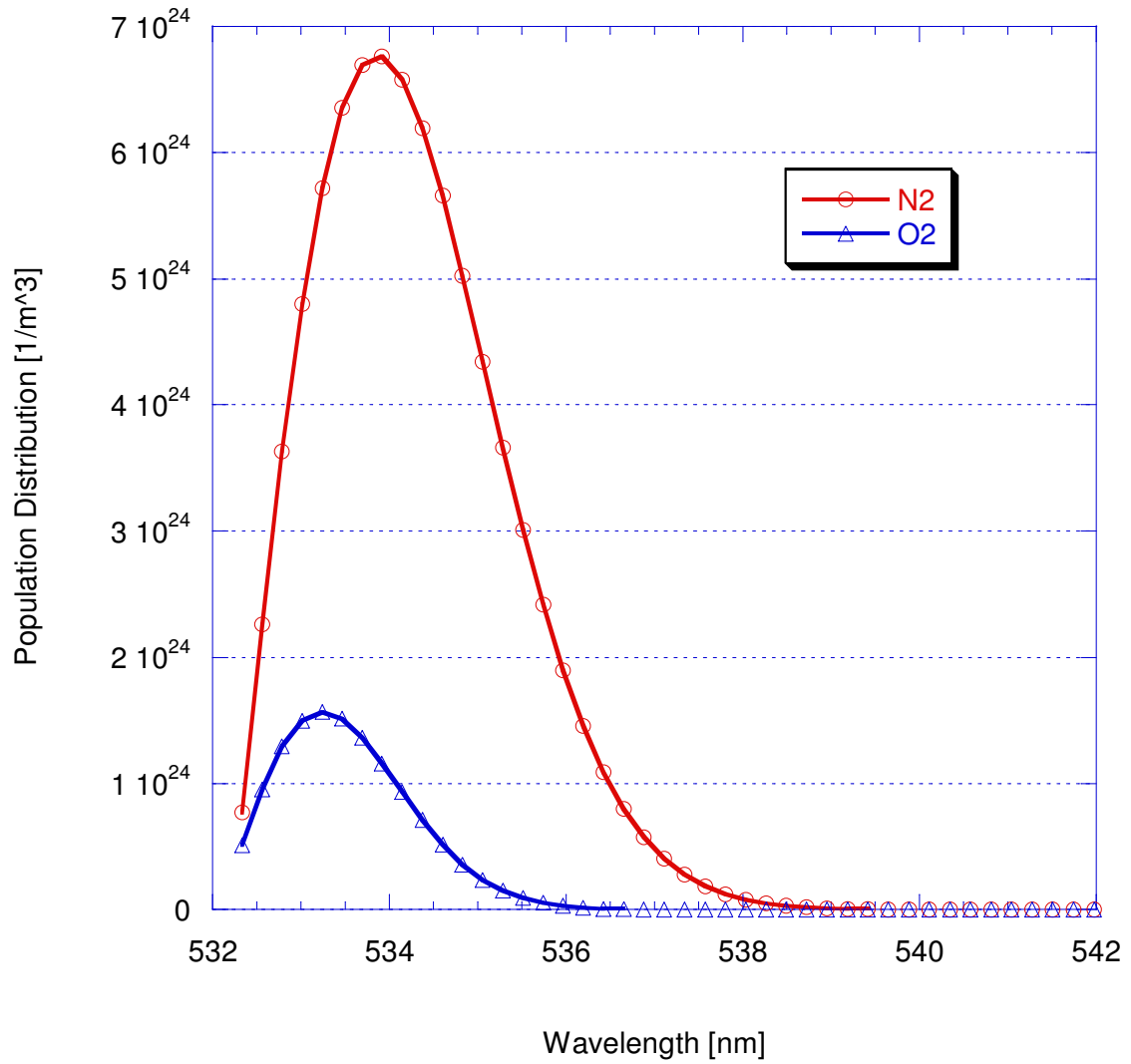
Fig. 4 Interpolated Rotational Stokes Profiles of Nitrogen and Oxygen at 300K
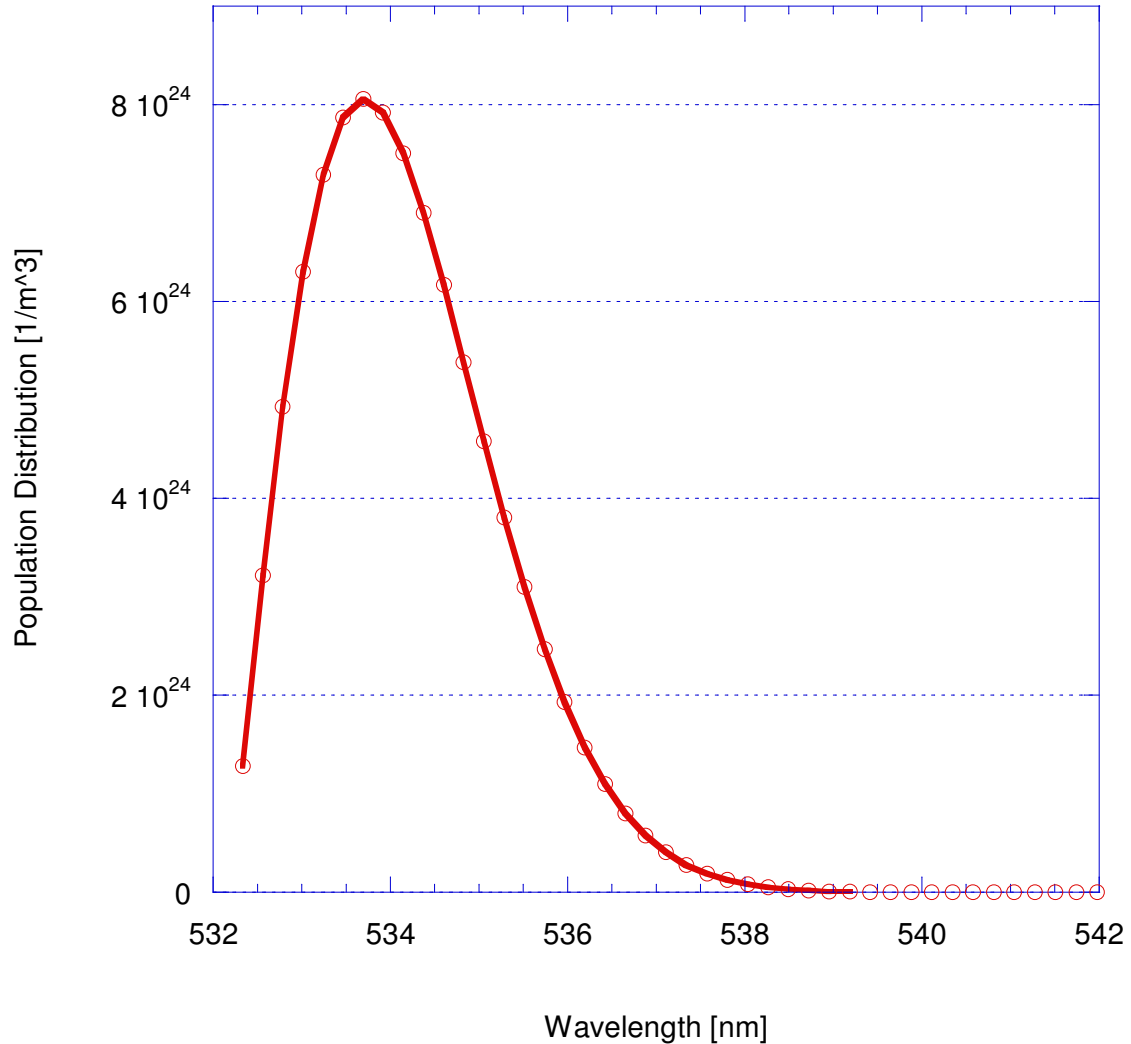
Fig. 5 Rotational Stokes Profile of Air at 300K

Once again, the individual points for each energy level cannot be seen due to the effects of line broadening. Therefore the profiles appear as smooth curves as seen in Fig. 6. It is observed that as temperature increases the maxima of the profiles decreases and shifts to higher wavelengths as part of an overall widening of the profile.
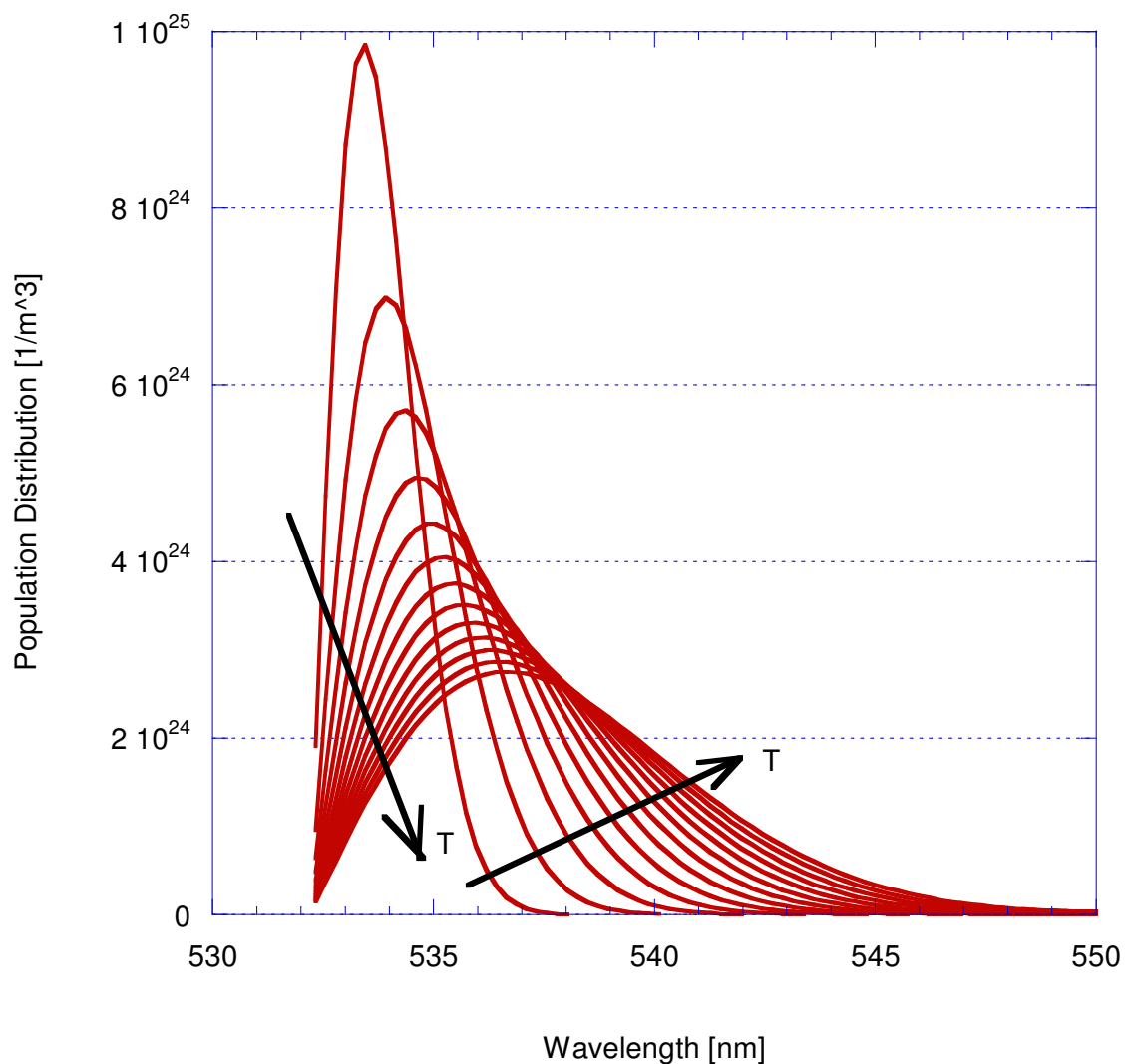
Fig. 6 Rotational Stokes Profiles of Air, 200K-2600K

The next step in forming the theoretical data tables is to degrade the resolution of the theoretical data to match the experimental resolution. This is done simply by taking the integration of the profiles. This process is applied to the integrated profiles shown in Fig. 7 so that the derivate can be taken later on.
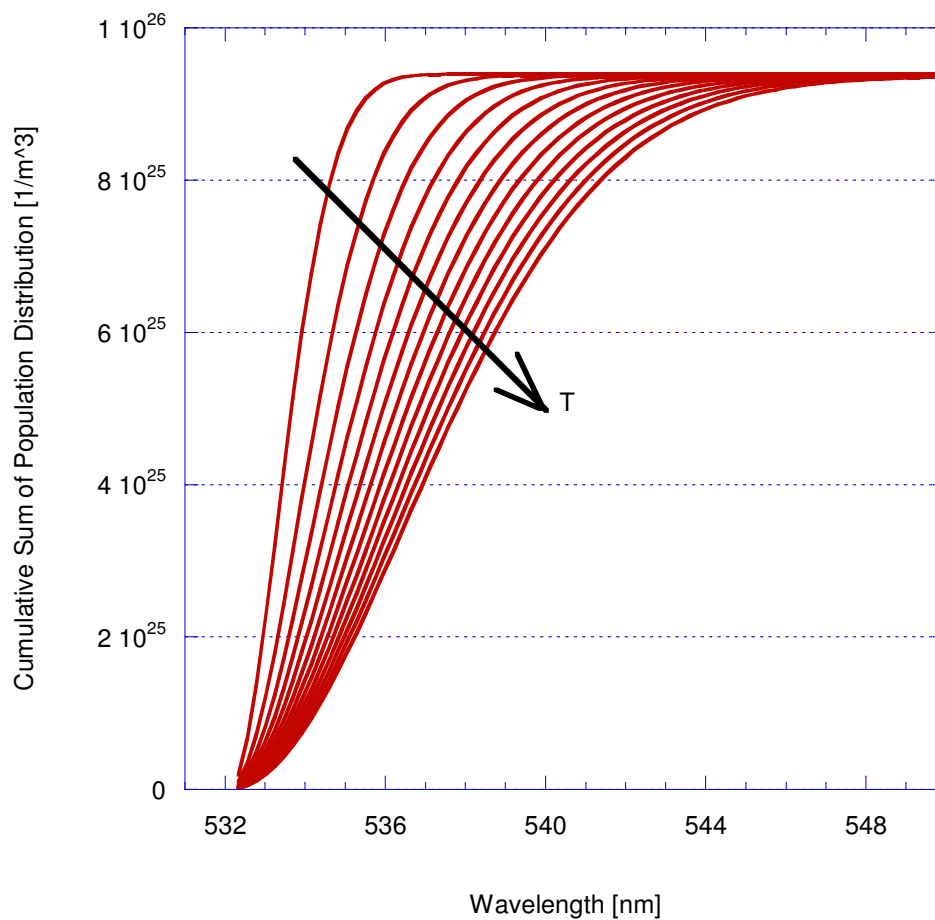
Fig. 7 Integrated Rotational Stokes Profiles of Air, 200K-2600K

This essentially takes a smooth curve and forms stepped sections as seen in Fig. 8. The resolution of Fig. 8 is approximately 1nm, which is equivalent to using 4x4 superpixel binning experimentally since the system has a resolution of 0.25nm/pix.
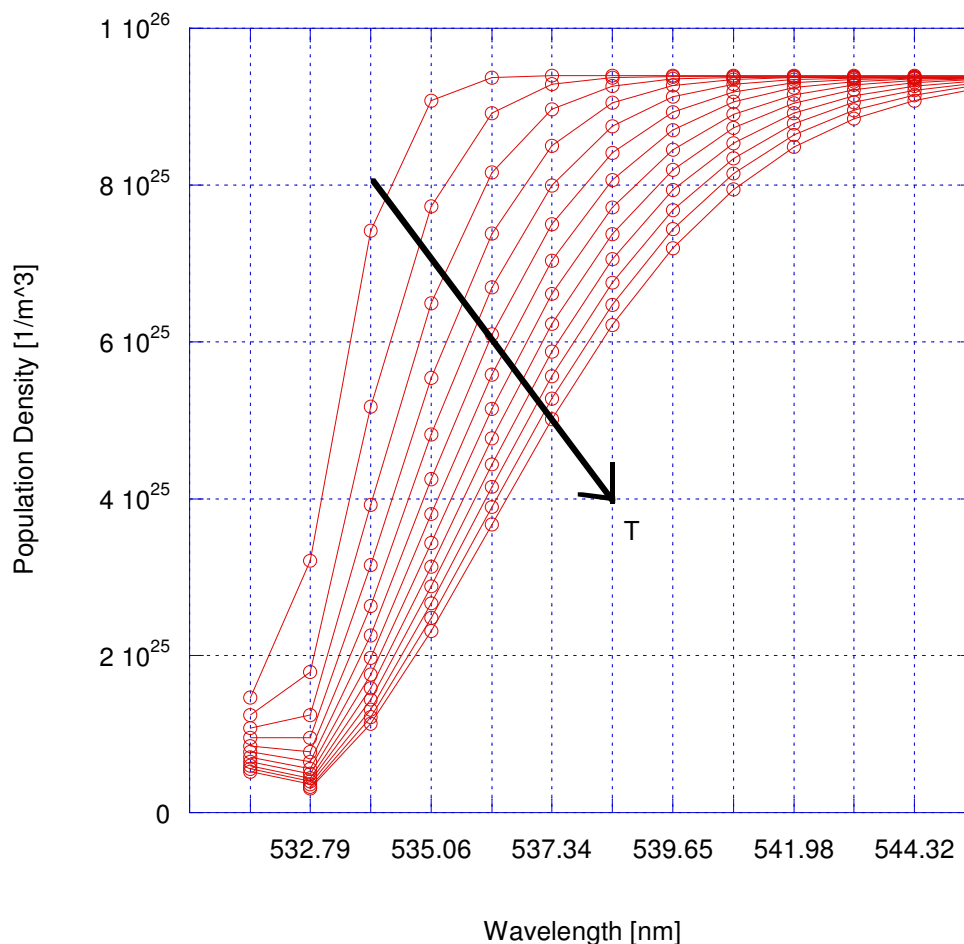
Fig. 8 Low Resolution Integrated Rotational Stokes Profiles of Air, 200K-2600K

The derivate is then taken and the resulting profiles plotted as shown in Fig. 9. As will be shown subsequently, these profiles are analogous to experimental profiles collected using 4x4 superpixel binning. Superpixel binning sums the signal from several pixels to create one large superpixel. Therefore, 4x4 superpixel binning sums the signal from a square region of 4 pixels high and 4 pixels wide and assigns that signal level to the 4x4 region. This serves to increase the signal-to-noise ration, S/N, at the expense of resolution.
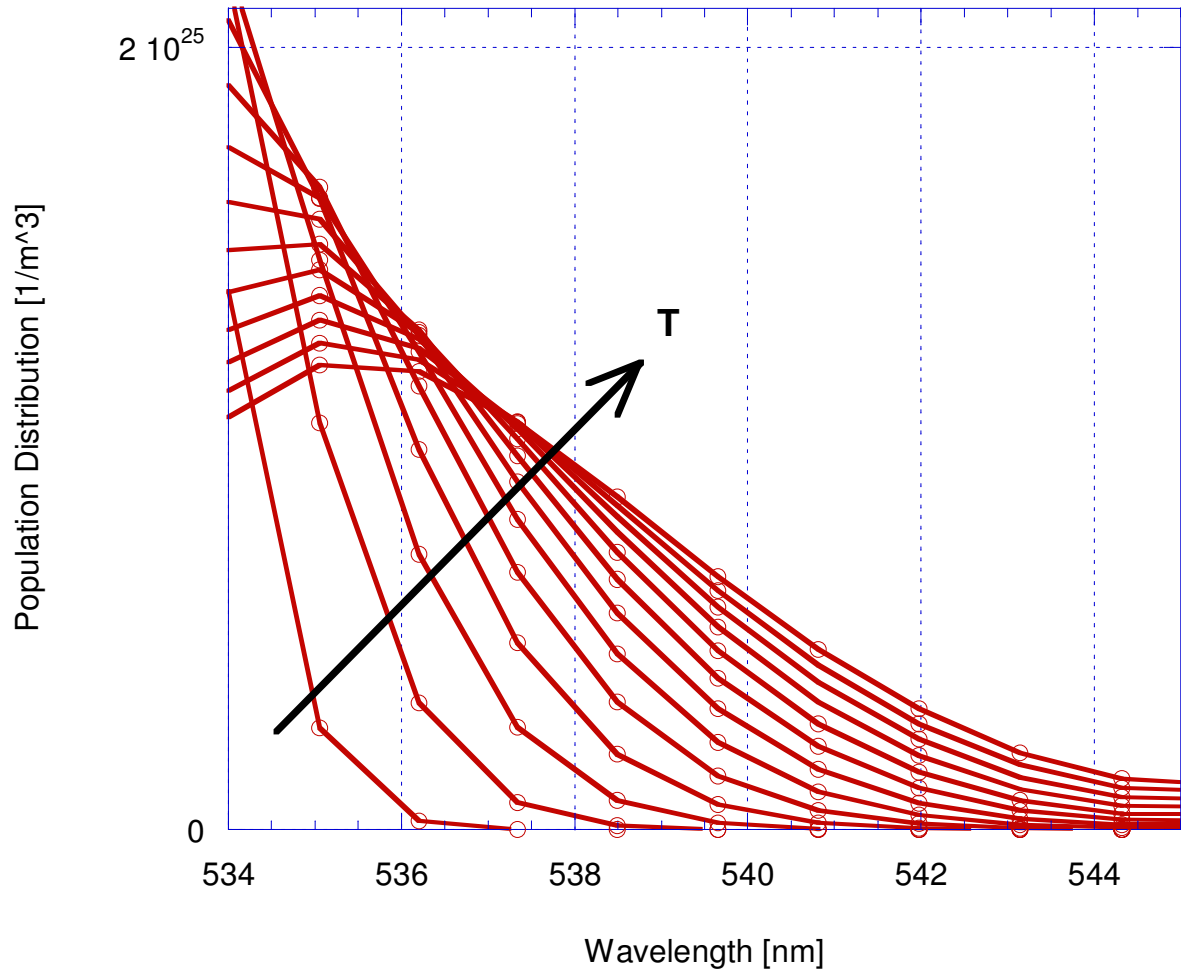
Fig. 9 Low Resolution Rotational Stokes Profiles of Air, 200K-2600K

Figure 10 shows the profiles plotted on logarithmic axes.
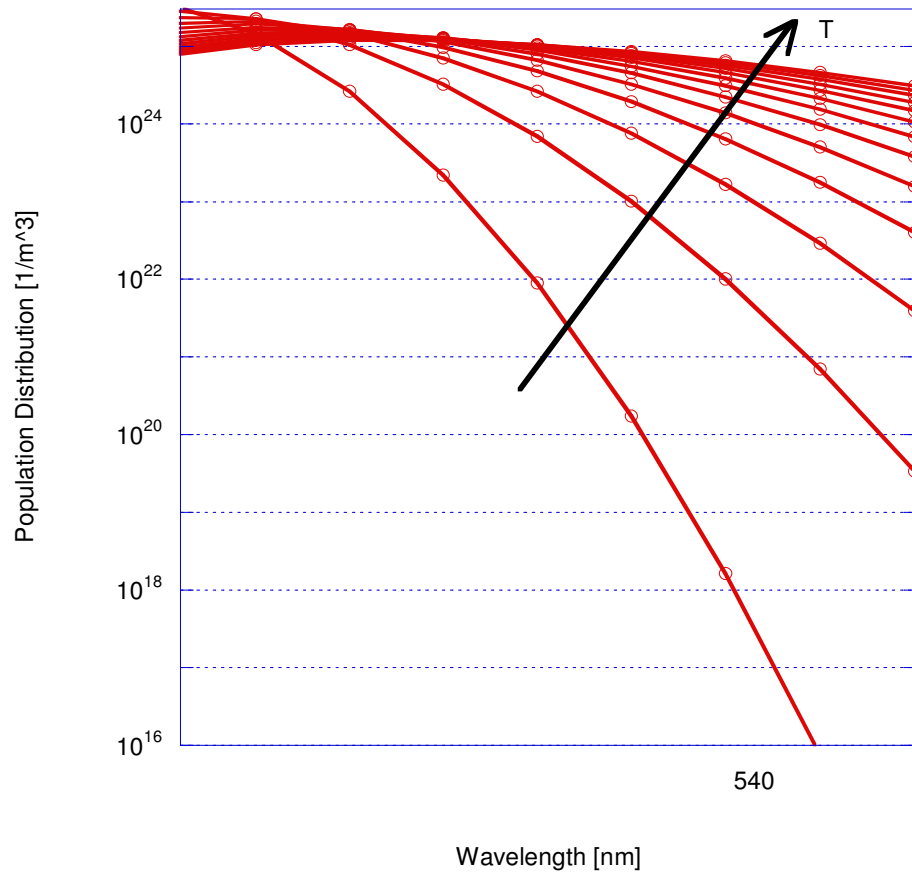
Fig. 10 Logarithmic Low Resolution Rotational Stokes Profiles of Air, 200K-2600K

With the experimental and theoretical profiles in equivalent form they can be compared numerically by using a least squares fit. The theoretical data can be generated at very small temperature intervals to improve precision of the comparison; 200K intervals were used here only for graphical clarity. In this manner the mixture temperature of a gas (air in this case) can be measured from the pure rotational spectrum. The process described thus far assumes known chemistry and composition (X_i). The laser diagnostic system described here is capable of more general measurements in flowfields where the chemical composition is not known *a priori*. The molar fractions,

X$_i$, can be measured in parallel by use of the vibrational Raman scattering as shown in the next section.

2.2 Rotational-Vibrational Raman

2.2.1   Rotational-Vibrational Raman Shifts

The Raman shifts, Stokes (red shift) and anti-Stokes (blue shift), for gas species can be calculated from quantum mechanical principles.
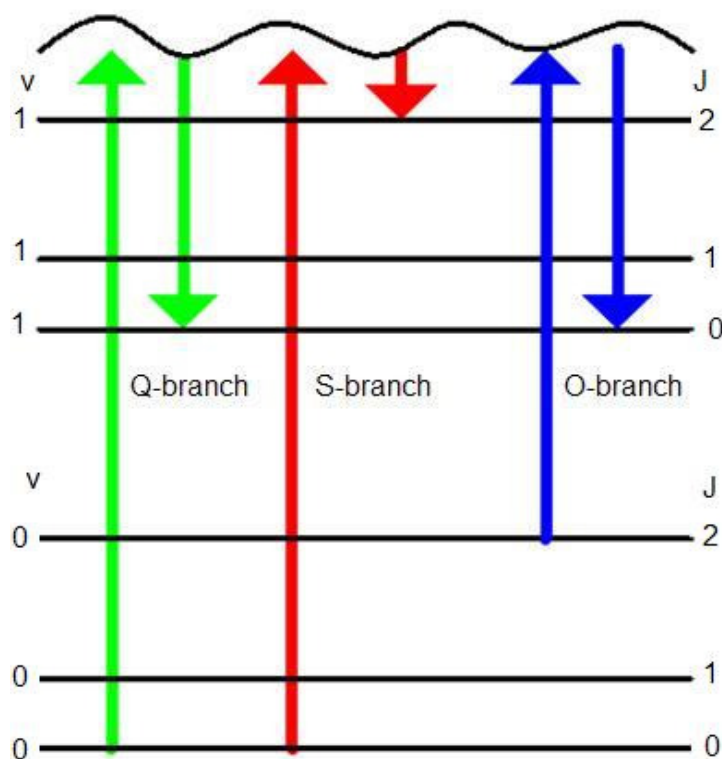
Fig. 11 Stokes Rotational-Vibrational Shift Energy Levels

Figure 11 shows the energy level shifts for the rotational-vibrational Stokes transitions. As with the rotational shifts, the molecule reaches a high virtual energy level before

settling at the final energy state. The Q-branch is a purely vibrational shift since there is no change in rotational energy. The S-branch is a rotational-vibrational shift with an increase in both vibrational and rotational energy, while the O-branch involves an increase in vibrational energy and a decrease in rotational energy. Similarly, the same branches can be associated with an anti-Stokes vibrational transition as shown in Fig. 12.
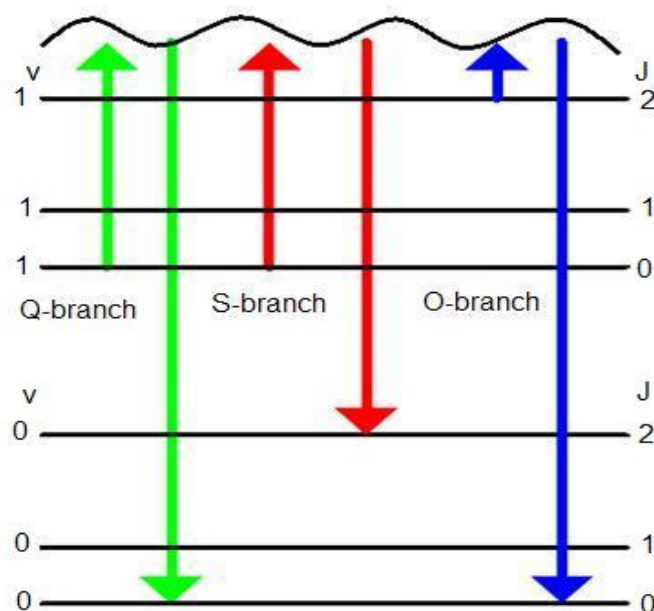
Fig. 12 Anti-Stokes Rotational-Vibrational Shift Energy Levels

To determine the shifted wavelength the frequency shift is first calculated, then added (anti-Stokes) or subtracted (Stokes) to the incident laser frequency. The Raman shift, or Raman frequency, is the magnitude of a Stokes or anti-Stokes shift for a particular gas. This magnitude is analogous to the distance between the energy levels at which the molecule may exist. These value have been tabulated in many works by laser diagnostic pioneers such as Eckbreth[13] and Lederman[15].

In an experimental setting the intensities of the spectral lines are used to extract properties of the gases being studied. The line intensities are proportional to the number of scatterers (molecules) of each species present. The signal of each species will appear at a unique wavelength (and intensity) and different physical locations on the collection CCD. The photon count is extracted from the energy scattered by each species. To find the photon count the total energy scattered by a species is divided by the energy of one scattered photon, which is dependent on the wavelength of that photon. The following calculates the wavelength at which a gas scatters light.

The scattering of light depends on the rotational constant, B, which is unique to each molecule. Equations (15)[15], (16)[15], and (17)[15] provide the change in wave number for the S, O, and Q branches, respectively, where J is the rotational quantum number, B' is the upper state rotational constant, and B'' is the lower state rotational constant. Δv_o is the vibrational Raman shift of the molecule and is available for constituents of air from both Lederman[15] and Eckbreth[13].

$$\Delta v_S = \Delta v_o + 6B' + (5B' - B'')J + (B' - B'')J^2 \qquad (15)$$

$$\Delta v_O = \Delta v_o + 2B' - (3B' + B'')J + (B' - B'')J^2 \qquad (16)$$

$$\Delta v_Q = \Delta v_o + (B' - B'')J + (B' - B'')J^2 \qquad (17)$$

Lederman has stated that the rotational constants (B) for the upper and lower states of a $0 \rightarrow 1$ vibrational transition are essentially equal[15] (B'=B''=B). This allows the above equations to be reduced to Equations (18), (19), and (20).

$$\Delta v_S = \Delta v_o + 6B + 4BJ \qquad (18)$$

$$\Delta v_O = \Delta v_o + 2B - 4BJ \qquad (19)$$

$$\Delta v_Q = \Delta v_o \qquad (20)$$

This entails that the Q branch spectral lines overlay[15], which increases signal strength and detection ability at the expense of resolution.

With the magnitude of the shift calculated, the shifted wavelength is easily found for the Stokes and anti-Stokes transitions by Equations (21) and (22) respectively (shown for the Q branch):

$$\lambda_{2Qs} = \frac{1}{\frac{1}{\lambda_1} - \Delta v_Q} \qquad (21)$$

$$\lambda_{2Qas} = \frac{1}{\Delta v_Q - \frac{1}{\lambda_1}} \qquad (22)$$

where λ_1 is the wavelength of the incident laser, λ_{2Qs} is the shifted Stokes wavelength, and λ_{2Qas} is the shifted anti-Stokes wavelength. The Stokes wavelengths for nitrogen and oxygen are 607nm and 580nm, respectively.

2.2.2 *Rotational-Vibrational Raman Spectroscopy*

The rotational-vibrational manifold is shifted considerably from the excitation wavelength, roughly 50-70nm in the case of air being excited at 532nm, so the ro0vib spectrum does not interfere with the pure rotational spectrum. While the temperature measurement is extracted from the decay of the Raman spectrum, the density is found from the intensity of the spectrum[13]. With the temperature and density known, the pressure is found through the equation of state.

The following derivation combines the phenomenological irradiance equation with the equation of state to obtain pressure. The phenomenological equation for irradiance due to vibrational Raman scattering of a single species is shown in Equation (23)[13], where I_{vib} is the scattered vibrational irradiance, ε is the efficiency factor of the experimental setup, I_o is the irradiance of the laser, Ω is the solid angle of the collection optics, l is the probe length, N is the number density, and $\left(\frac{\partial \sigma}{\partial \Omega}\right)_{vib}$ is the vibrational scattering cross section of the species.

$$I_{vib} = \varepsilon I_o \Omega l N \left(\frac{\partial \sigma}{\partial \Omega}\right)_{vib} \qquad (23)$$

Equation (24) is the state equation where P_i is the partial pressure of each species, v_i is the species mass specific volume, R_i is the species specific gas constant, and T_m is the temperature of the mixture (subscript m denotes mixture throughout the derivation). For a mixture of gases the temperature is equal for the mixture and all constituent species[19].

$$P_i v_i = R_i T_m \tag{24}$$

Since the species specific gas constant is the universal gas constant ($\bar{R}$) divided by the molar mass of the species ($\overline{M}_i$) the state equation can be written as Equation (25).

$$P_i \frac{V_m}{M_i} = \frac{\bar{R}}{\overline{M}_\iota} T_m \tag{25}$$

Solving for the partial pressure of each species, P_i, and using the definition of number of moles of a species $n_i = M_i / \overline{M}_i$ Equation (26) is formed.

$$P_i = n_i \frac{\bar{R} T_m}{V_m} \tag{26}$$

The number density of a species, N_i, is defined by Equation (27), which also substitutes the results of Equation (26) to relate N_i to P_i.

$$N_i = \frac{P_i}{\overline{\overline{R}} T_m} \tag{27}$$

The vibrational Raman scattering cross section, Equation (28)[13], is mainly dependent on the frequency shift shown in the numerator and also the temperature, which appears in the Boltzmann vibrational partition function, $\left(1 - e^{-hc\frac{\omega_e}{kT_m}}\right)$, seen in the denominator .

$$\left(\frac{\partial \sigma}{\partial \Omega}\right)_{ram,i} = \frac{h(v_o - v_{k,i})^4 \left((\alpha')^2 + \left(\frac{4}{45}\right)(\gamma')^2\right)}{8\overline{M}_i c^4 v_{k,i} \left(1 - e^{-hc\frac{\omega_e}{kT_m}}\right)} \tag{28}$$

In Equation (28) h is Planck's constant, c is the speed of light, k is the Boltzmann constant, v_o is the wavenumber of the excitation frequency, $v_{k,i}$ is the wavenumber of the Stokes shift, and ω_e is the oscillation frequency over the speed of light[15]. The term $\left((\alpha')^2 + \left(\frac{4}{45}\right)(\gamma')^2\right)$ in the numerator relates to the polarizability of the molecule where α' and γ' are invariants of the polarizability tensor[13]. While it is possible to calculate the scattering cross sections from Equation (28), it is rather involved and unnecessary since the cross sections for many common molecules have been found experimentally. Tabulations[13] provide values of $\left(\frac{\partial \sigma}{\partial \Omega}\right)_{ram,i}$ for specific excitation wavelengths, and the data is corrected for different values by using the forth power factor, $(v_o - v_{k,i})^4$, shown in Equation (28).

The species number density and Raman scattering cross section are then substituted into Equation (23) to produce a relationship between measured irradiance, pressure, and temperature of a species. Equation (29) shows the result of this substitution solved for partial pressure.

$$P_i = \frac{I_i \overline{R} T_m}{I_o \Omega l \varepsilon} \left[\left(\frac{\partial \sigma}{\partial \Omega} \right)_{ram,i} \right]^{-1} \qquad (29)$$

The pressure of a mixture of gases is the summation of the partial pressures of each species[19]. Therefore, Equation (29) can be reconstructed to measure the mixture pressure by summing the scattering cross sections and measured irradiances while also accounting for species concentrations as seen in Equation (30), where I_t is the total measured irradiance (summed over all species) and X_i is the mole fraction of each species.

X_i is known for air, but is unknown generally. The measurement of X_i is accomplished by examining $X_i \left(\frac{\partial \sigma}{\partial \Omega} \right)_{ram,i}$, which is proportional to the photon count at different wavelengths, i.e. different regions of the CCD. Since the scattering cross section is known, X_i can be measured in every location of the linear laser probe volume.

$$P_m = \frac{I_t \overline{R} T_m}{I_o \Omega l \varepsilon} \left[\sum_i X_i \left(\frac{\partial \sigma}{\partial \Omega} \right)_{ram,i} \right]^{-1} \qquad (30)$$

Using the temperature measured from the rotational spectrum and experimental data from rotational-vibrational scattering, Equations (29) and (30) can provide a measurement of pressure.

3. EXPERIMENTAL APPARATUS

3.1 Laser

The rotational-vibrational Raman spectroscopy system assembled for this research employs a Class IV Nd:YAG laser from Continuum (Powerlight Precision II 8010). The laser's fundamental frequency (1064nm) is doubled to a wavelength of 532nm (green), delivering approximately 800mJ to the test section with 5-7ns pulse width at a frequency of 10Hz. The laser power is crucial since the magnitude of the scattered light is proportional to the laser power as shown in Equation (23).

3.2 Telescope

Dielectric breakdown occurs when a nonconductive material becomes conductive through ionization. In lasers, a strong beam focused to a small waist (creating a large electric field) can cause a dielectric breakdown in air, resulting in sparks[20]. This is detrimental to spectroscopy due the sensitivity of the camera; a spark can burn the CCD and impair measurements. The electric field that a nonconductive material can withstand before dielectric breakdown is known as the dielectric strength, which is approximately $3x10^6$ V/m for air[20]. This corresponds to a power distribution of $0.35x10^{12}$ W/cm$^{2(13)}$, which is a more useful quantity for determining if a particular laser system will cause dielectric air breakdown. With 0.8J of energy, pulse duration of 6ns, and a beam waist (diameter) of 250μm, the cross-sectional power distribution of the beam is calculated to be $0.272x10^9$ W/cm^2, which is well below the threshold value. The

250μm beam waist is known from previous research using similar lasers by Karpetis and Barlow[11]. Equation $(31)^{13}$ calculates the diameter of the diffraction limited beam waist where f is the focal length of the lens, D is the beam diameter at the lens, and λ is the wavelength of the laser beam. Equation $(32)^{13}$ defines the angle of diffraction at which a beam is considered diffraction limited. The actual beam waist is an order of magnitude greater than the diffraction limited beam waist of 41μm since the laser beam is uniform rather than Gaussian.

$$d_{lim} = \frac{2.44f\lambda}{D} \tag{31}$$

$$\theta_{lim} = \frac{2.44\lambda}{D} \tag{32}$$

A common cause of dielectric breakdown is a non-uniform beam cross-section containing "hot spots", or regions of higher energy. These hot spots can create an electric field greater than air's dielectric strength. One method for eliminating this problem is to pass the beam through a Galilean telescope before focusing in the test section. The Galilean telescope consists of a concave objective lens (negative focal length) and a plano-convex lens (positive focal length). The increase in beam diameter results in a more uniform profile of intensity, but this occurs at the cost of a smaller beam waist.

Ray tracing is used to calculate the telescope parameters in order to expand the beam as much as possible within the given optics. It is desirable to have the beam collimated after the telescope, so that the focusing lens operates at the design focal length (750mm in this case).

A ray impinges upon a surface (lens in this case) at an angle θ and distance from the optical axis (beam radius) ρ. Subscripts are taken as 1 when impinging the lens and 2 when leaving. In the telescope system with two lenses the second lens has subscripts of 3 and 4, with the angle impinging upon the second optic equal to the exiting angle from the first lens. The transformation matrix, known as the ray matrix, is defined for commonly encountered optics. For the Galilean telescope there are two types of optical elements involved: the thin lens and a homogenous medium (air). Table 1 provides the ray matrices for these two elements[21].

Table 1   Ray matrices for thin lens and homogenous medium

Thin Lens	Homogenous Medium
$\begin{bmatrix} 1 & 0 \\ -1/f & 1 \end{bmatrix}$	$\begin{bmatrix} 1 & d \\ 0 & 1 \end{bmatrix}$

In the above ray matrices f is the lens focal length and d is the distance traveled through the medium (the distance between the two lenses). Equations (33), (34), and (35) show the ray equations for a thin lens of focal length f_1, an open space in air of distance d, and a second lens of focal length f_2, respectively.

$$\begin{bmatrix} \rho_2 \\ \theta_2 \end{bmatrix} = \begin{bmatrix} 1 & 0 \\ -1/f_1 & 1 \end{bmatrix} \begin{bmatrix} \rho_1 \\ \theta_1 \end{bmatrix} \tag{33}$$

$$\begin{bmatrix} \rho_3 \\ \theta_3 \end{bmatrix} = \begin{bmatrix} 1 & d \\ 0 & 1 \end{bmatrix} \begin{bmatrix} \rho_2 \\ \theta_2 \end{bmatrix} \tag{34}$$

$$\begin{bmatrix} \rho_4 \\ \theta_4 \end{bmatrix} = \begin{bmatrix} 1 & 0 \\ -1/f_2 & 1 \end{bmatrix} \begin{bmatrix} \rho_3 \\ \theta_3 \end{bmatrix} \tag{35}$$

In the above equations $\rho_1=\rho_2$ and $\rho_3=\rho_4$ since a thin lens is treated as a plane. A change in beam size is accomplished by a refracted ray traveling over a distance d. Therefore the beam enters and leaves a lens at the same height, the purpose of the lenses being to refract the light. Similarly, $\theta_2=\theta_3$ since the light will not refract over the distance d.

In this particular application, it is desired for the telescope to expand the beam to the greatest width possible for the given optics while maintaining collimation upon exiting the telescope. Therefore, several of the variables in the ray equations are known and fixed, reducing the problem considerably. ρ_1 is the radius of the beam entering the first lens, which is the same as exiting the laser. This is determined by the size of the rod in the laser's oscillator, which in this case is 9mm in diameter, therefore setting $\rho_1=4.5$mm. The light from the laser is collimated, therefore θ_1 is zero. Similarly, θ_4 is also zero since the exiting light should be collimated. The lenses chosen for the telescope are 25mm in diameter, so the desired exiting beam diameter was chosen to be

24mm (nearly filling the optic), fixing ρ_4 at 12mm. Using these constraints and relations the ray equations are simplified to Equations (36), (37), and (38).

$$d = \frac{\rho_4 - \rho_1}{\theta_2} = \frac{\rho_4 - \rho_1}{-\rho_1/f_1} \tag{36}$$

$$f_1 = {}^{-\rho_1}/{\theta_2} \tag{37}$$

$$f_2 = {}^{-\rho_4}/{\theta_2} \tag{38}$$

Solving the system simultaneously in terms of f_1 results in the simple relations shown in Equations (39) and (40):

$$d = -\frac{5}{3}f_1 \tag{39}$$

$$f_2 = -\frac{8}{3}f_1 \tag{40}$$

It was found that using an objective lens (f_1) with focal length of -300mm, an eyepiece (f_2) of focal length 400mm, and separating them by 200mm (d) yields the desired results with readily available lenses and manageable spacing. Table 2 shows the parameters of the system using some common focal lengths for f_1.

Table 2   Telescope parameters

f_1 [mm]	f_2 [mm]	d [mm]
-500	666.6667	333.3333
-300	400	200
350	-466.667	-233.333
500	-666.667	-333.333
750	-1000	-500

The optics used must be selected not only based on achieving the desired beam size and collimation, but also on realistic lenses and allowable distances. Lenses, for instance, are usually ground to round numbered focal lengths, such as -300mm, 500mm, etc.; therefore a lens of focal length -466.667mm is not practical. Also, the laser beam travels a finite distance from the laser to the test section. This fact and the additional necessary optics in the system (turning mirrors, focusing lens, etc.) limit the space available in which to set up a telescope.   The parameters of this telescope are f_1=-300mm, f_2=500mm, and d=400mm.

3.3 Pulse Stretcher

The telescope was not sufficient for the elimination of dielectric breakdown in the test section. This means that the hot spots in the beam, which the telescope is supposed to resolve, were not the dominant reason for sparking, but rather the presence of dust in the laboratory, leading to laser light absorption and dielectric breakdown. In the present work a pulse stretcher was utilized to distribute the laser power over a longer period of time. This pulse stretcher consists of a beam splitter and several mirrors. The

incoming beam passes through the beam splitter which transmits part of the beam while reflecting the rest. Beam splitters come in different variations, with 50/50 or 30/70 (how much of the beam is reflected or transmitted) being most common; a 50/50 beam splitter is used for this system and is set at 45 degrees to the incident beam.

The beam splitter is positioned at an angle to the incident beam so that the reflected portion of the beam is directed away from the incident beam. It is dangerous to send reflections back into the laser as it might destroy the laser's rod and reflections from the beam splitter must be carefully controlled. The reflected portion of the beam is directed to a path towards a mirror and reflected to another mirror that will send the beam back to the beam splitter to recombine with the incident beam. This is a physical delay system, the magnitude of which depends on the length of the pulse stretcher's leg. The delay time is simply calculated by dividing the total length of the leg by the speed of light. This particular pulse stretcher has a 4ft distance between mirrors, so the light travels 8ft and is delayed by approximately 8ns (speed of light is approximately 1ft/ns) The pulse stretcher is depicted in Fig. 13.
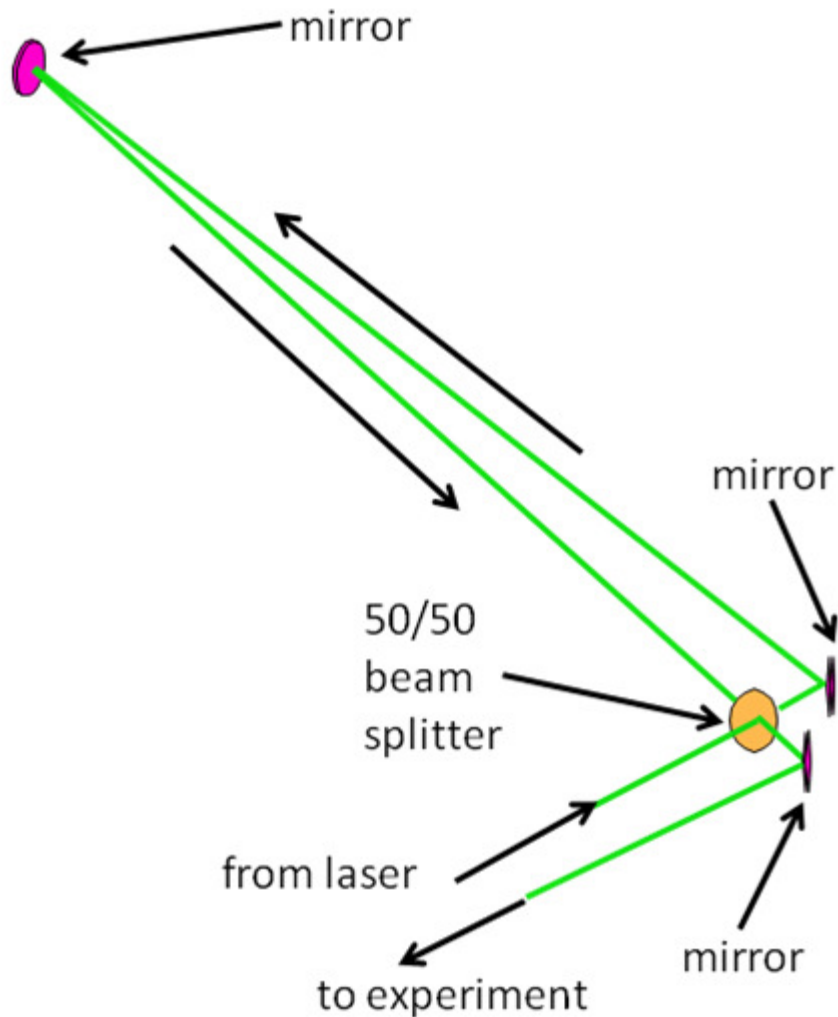
Fig. 13 Pulse Stretcher

The incident and reflected/delayed beams interfere with each other upon recombination. This serves to split the original laser pulse into a number of lower energy pulses, each delayed by a small time, and recombine them into a broader pulse. The end result is a laser pulse that has a lower maximum and a wider width, thus reducing the laser flux and likelihood of dielectric breakdown. This pulse stretcher takes the 5-7ns pulse from the laser and stretches it to approximately 20ns full width at half

max (FWHM). It was this pulse stretcher that reduced the sparking of the system to a workable level. Previously, it had been sparking with every shot.

3.4 Spectrometer

A spectrometer is the device used to collect diffracted light for analysis. Collection optics, a diffraction grating, and some means to record the collected light are needed. Current technology spectrometers use reflective diffraction gratings and CCD arrays to diffract and record the spectra, respectively. Self contained spectrometers of this nature are available commercially and are the standard in most spectroscopy labs. The spectrometer developed here is unique in that it was designed and constructed in-house specifically for this research and utilizes a new volume phase holographic (transmissive) grating. Figure 14 pictures the spectrometer with the components labeled.
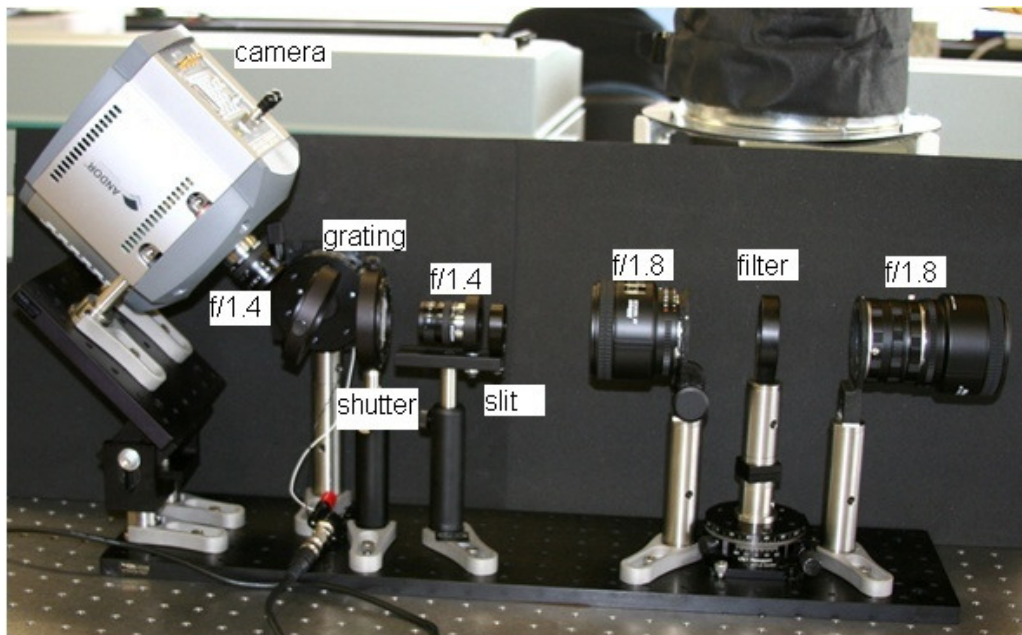
Fig. 14 Spectrometer Components

3.4.1 Light Collection and Filtering

At the test section, where the beam focused, the first collection lens is positioned perpendicularly to the beam. In Fig. 14 the first lens, Nikkor f/1.8 at the right of the photograph, is situated at its focal length from the beam (85mm in this case). The f-number is defined as the ratio of the focal length to the diameter of the lens. Placing the lens at its focal length from the beam causes the light to be collimated (focused at infinity) upon exiting the lens. While the Nikkor uses a complex series of lenses the thin lens approximations (Equation (41)) valid, are applied to obtain the effective lens diameter (d_l) of 47.22mm at the lens iris.

$$d_l = \frac{f}{f_\#} \qquad (41)$$

The Raman scattered energy is proportional to the solid angle of the collection optics, making the f-number and focal length of the collection lenses extremely important. It is ideal to have low f-number ("fast") lenses to get larger solid angles and collect more light. The solid angle (Ω) is a three dimensional angle subtended by the lens aperture positioned at the focal distance of the lens. An isosceles triangle can be formed with the lens diameter as the base and the focal length as the height. The basic trigonometry shown in Equation (42) is used to calculate the half angle (θ), which is

15.52°.   Figure 15 shows the geometry with dimensions (linear dimensions in millimeters) used in the calculations.

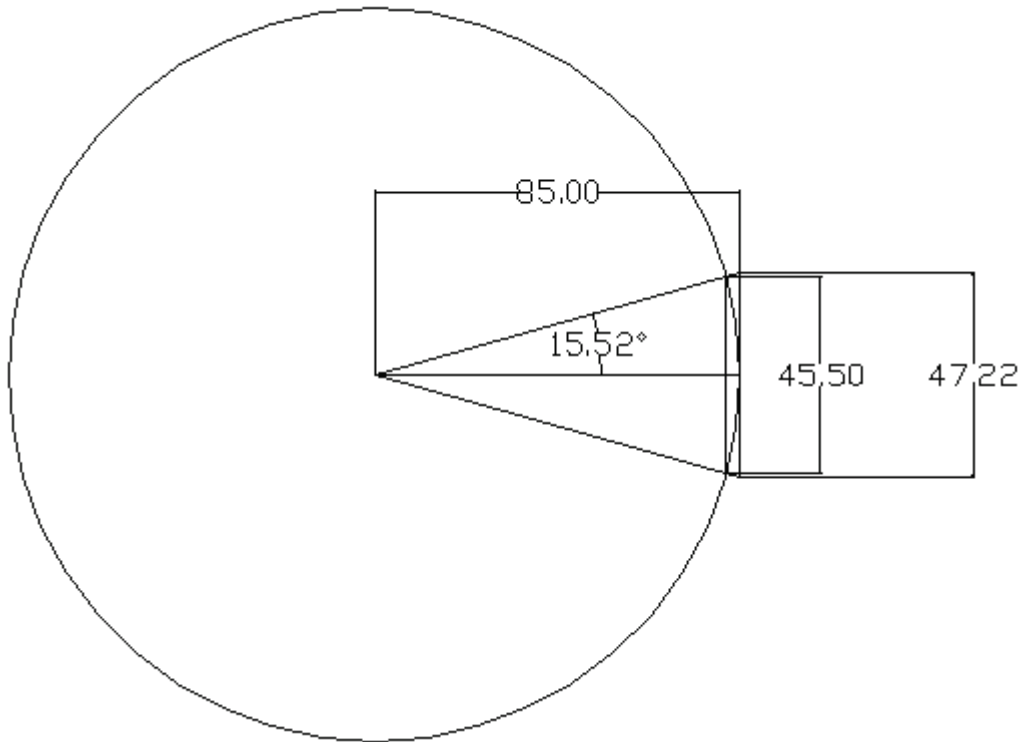**Fig. 15 Geometry for Solid Angle Calculation**

$$\theta = \tan^{-1}\frac{d_l}{2f} \tag{42}$$

The solid angle is then calculated by integrating the sine of the half angle with respect to itself and with respect to an angle φ which corresponds to the circular projection over 2π radians. Evaluating Equation (43) results in a solid angle of 0.229sr (steradians), which is still a small portion of a sphere (4πsr).

$$\Omega = \int_0^{2\pi} \int_0^{\theta} \sin\theta \, d\theta \, d\phi \tag{43}$$

The specifications of the first set of doublet lenses play a crucial role in the spectrometer. With the low signal levels of Raman scattering every pain is taken to collect as much light as possible. Between the first set of doublet lenses the long-pass filter is mounted. The purpose of the filter is to block the Rayleigh scattered light, which occurs at the incident wavelength (532nm). The Rayleigh signal is roughly three orders of magnitude stronger than the vibrational Raman signal[13], so it must be filtered out or else it will wash out the Raman signal.

To block the Rayleigh signal the Semrock RazerEdge long-pass filter is used. This is an extremely sharp filter that blocks light of wavelengths 532nm or less, while at the same time allowing longer wavelengths to pass through. The response curve for the long-pass filter is shown in Fig. 16, where it is clear that the filter's transmission changes from practically zero to nearly 100% of the light over a Δλ≈1nm band approximately centered at 536nm.
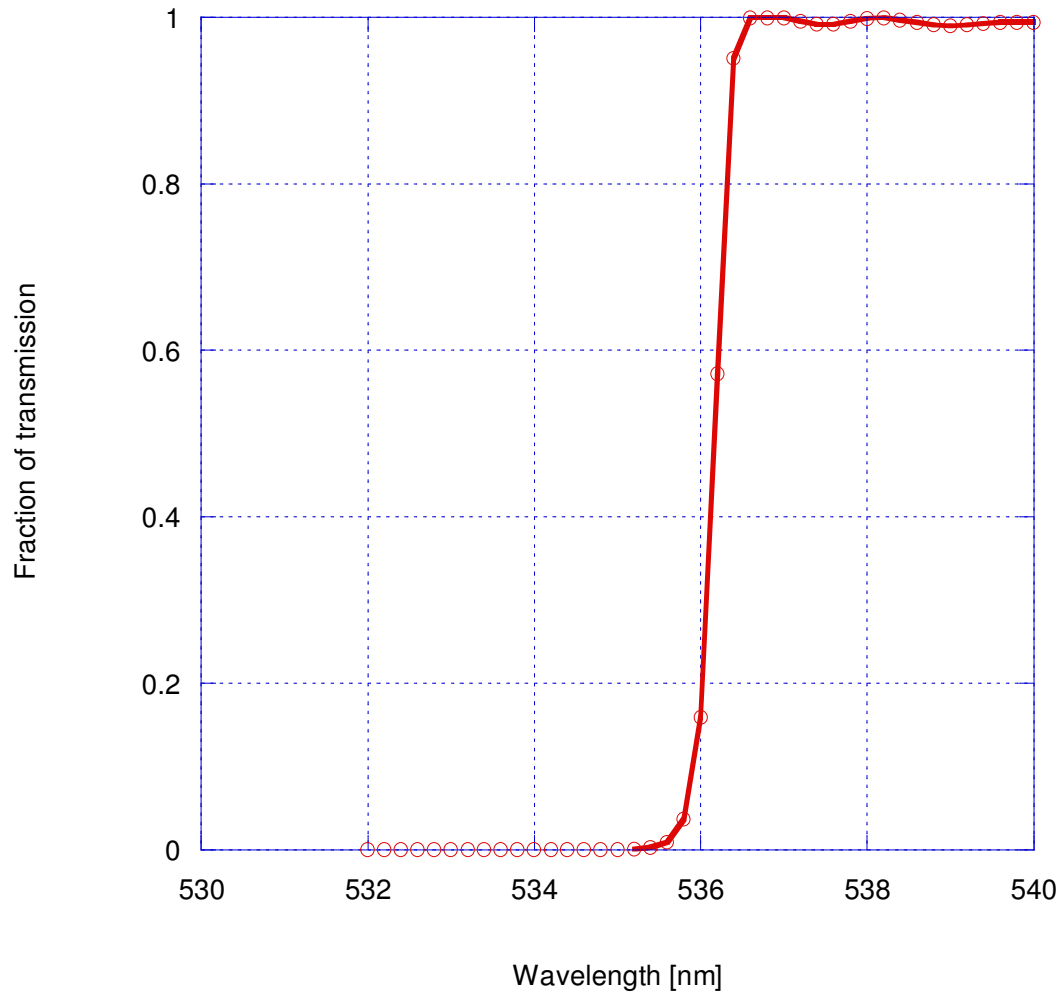
Fig. 16 Long-pass Filter Response

While the filter's cutoff is very sharp, the wavelength at around 536nm is not desirable because it would still result in the elimination of a large portion of the pure rotational spectrum. To mitigate for this loss, the filter's cutoff wavelength can be

adjusted by rotating the filter about its vertical axis so that the incident angle of the collimated light changes. Equation (44) calculates the cutoff wavelength (λ) as a function of the filter's incident angle (θ) where n_{eff} is the effective refractive index and λ_o is the incident wavelength. This equation and the effective refraction indices were obtained from the filter manufacturer[22].

$$\lambda = \lambda_o \left(1 - \left(\frac{sin\theta}{n_{eff}} \right)^2 \right)^{1/2} \tag{44}$$

Plotting the data generated by Equation (44) shows that for 90% transmission and vertical polarization (same as the laser) the filter cutoff can be brought as low as 534nm by rotating the filter by 10 degrees. Fig. 17 shows the transmission of the Semrock filter as a function of rotation. By rotating the filter to 10 degrees a significant portion of the purely rotational Raman spectrum is captured.

Fig. 17 Semrock long-pass Filter Rotation

Fig. 18 Rotational Profile Cutoff with 10 Degree Filter Rotation

Figure 18 shows the affect on the rotational profile of rotating the filter to 10 degrees. A significant portion of the Boltzmann decay of the rotational spectra is permitted and unaffected by the filter, while the Rayleigh scattering (elastic) at 532nm is rejected as intended.
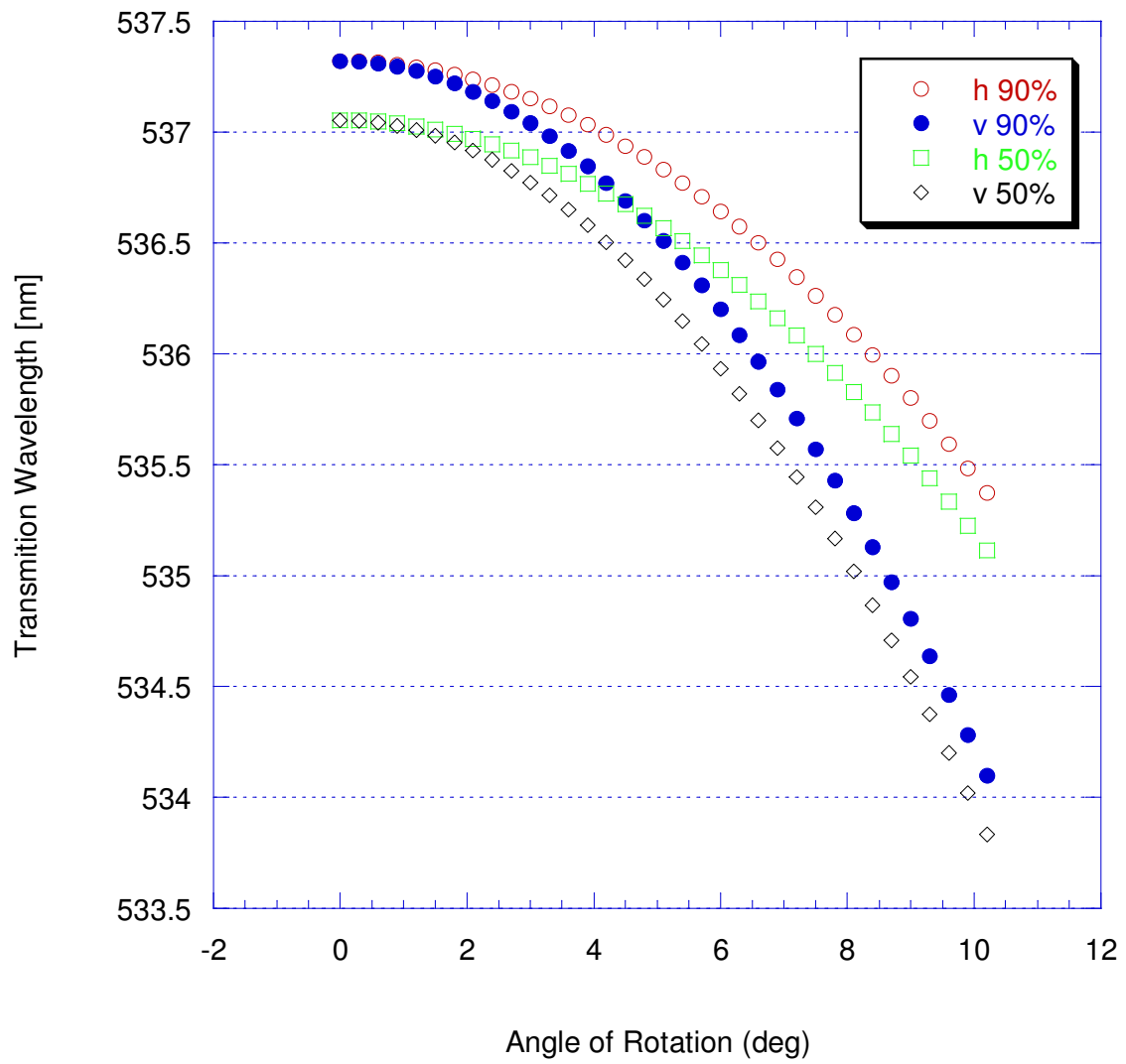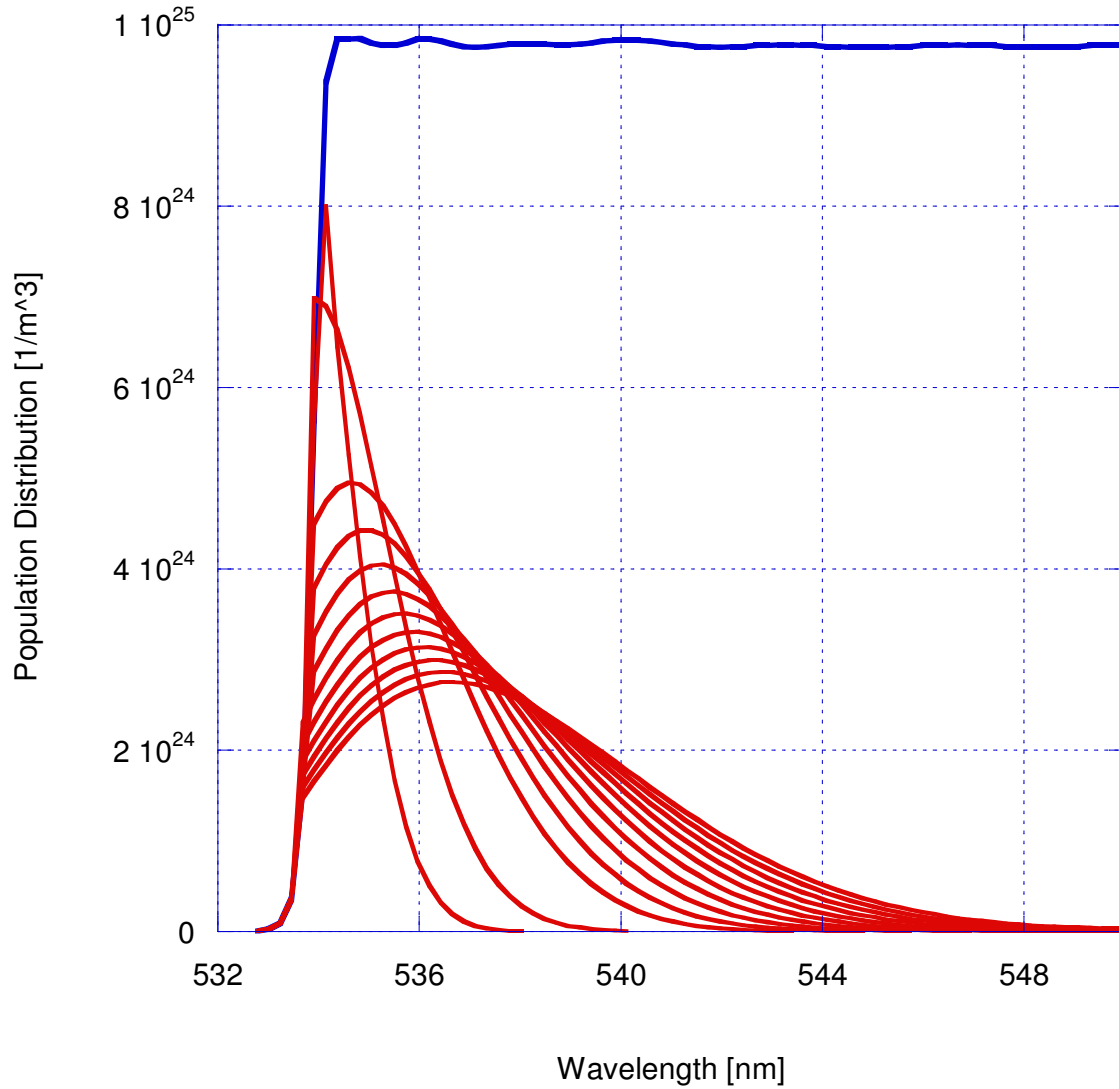
The second lens in the first doublet set focuses the light onto a rectangular slit of 250 micron width. This slit defines the probe volume that is imaged onto the CCD and blocks extraneous light. With the beam focused in the test section the portion of it collected by the f/1.8 doublet is not rectangular. Rather, the shape converges and diverges as the beam reaches its waist. By passing through the slit, only a uniform, rectangular section of the beam is captured on the CCD. With an expected beam waist of 250μm, this spatial filtering results in elimination of most background light from ambient sources.

3.4.2   Shutter

Minimizing ambient light interference is vital to obtaining high quality data. When using a pulsed laser ambient light still enters the optical system between laser pulses. To collect as little ambient light as possible a shutter is used that blocks light collection during the time intervals between laser pulses.

The shutter (Displaytech LV2500P-DEM) is a ferroelectric liquid crystal (FLC) device of one inch diameter that employs an applied voltage to alter the polarization of the optic. The FLC is mounted between two polarizers that either block or allow the passage of light depending on the polarity of the applied voltage. The application of voltage is controlled via a driver that allows the shutter to permit light passage at specified rates and durations on the order of tens of microseconds. Through testing using white light sources it was found the optimal cycle time, to go from totally closed to totally open to totally closed (or vice versa), to be 120 microseconds. This value is still

much longer than the laser pulse duration (~20ns), thus allowing some background light to be collected onto the CCD. Still, this gate eliminates most of the background during the inter-pulse period of 100ms.

3.4.3 Grating

In order to perform spectroscopy, the image of the laser probe, convolved by the slit, must be introduced into a second lens system that introduces 'symmetry breaking' into the imaging operation by using a diffraction grating (see Fig. 14). When passing through a diffraction grating each wavelength is diffracted at a different angle, spreading the spectrum in space so that individual wavelengths can be seen. Therefore, when collecting light on a CCD each wavelength will focus in a different location on the CCD.

A reflective diffraction grating is a grooved reflecting surface upon which light is incident. The groove spacing determines the dispersion of the device and quality of the light diffracted; the smaller the groove spacing (generally given in grooves per millimeter) the finer the grating. The grooves are generally cut at an angle, known as the blaze angle; these gratings are also referred to as blazed gratings[23] or surface relief gratings.

For this research a transmissive grating, or volume phase holographic grating, is used. A transmissive grating is an optic that diffracts light passing through it, rather than reflecting off of it as is the case with surface relief gratings. This grating (Wasatch Photonics 1269-03) has a light transmission of approximately 95%, as opposed to the ~60% transmission of reflective gratings. The volume phase grating consists of a

dichromate gelatin grating mounted between two panes of glass. The index of refraction of the gelatin varies periodically throughout the grating and is responsible for diffraction. The varying index of refraction acts as the grooves of a surface relief grating and is generally described by the same groove frequency (or its inverse in grooves per millimeter). Figure 19 depicts a cross-section view of a volume phase grating where d is the groove spacing, and the incident and diffracted angles are marked with subscripts "i" and "d", respectively.
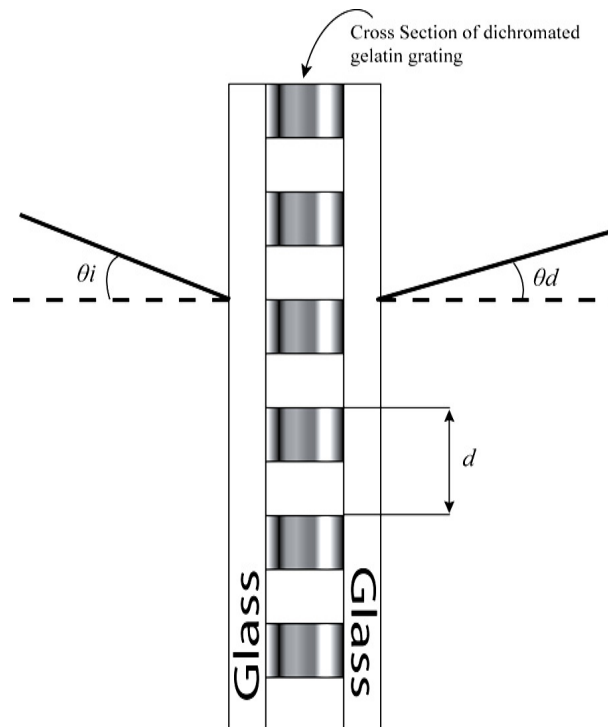
Fig. 19 Volume Phase Grating Cross Section

The standard grating equation applies to both surface relief gratings and volume phase gratings. In Equation (45)[24] θ_d is the diffracted angle, θ_i is the incident angle, n is

the order of diffraction (generally 1, the strongest order), λ is the incident wavelength, and d is the dispersion.

$$sin\theta_d = \frac{m\lambda}{d} - sin\theta_i \qquad (45)$$

From the grating equation it is easy to calculate the diffraction angle for each wavelength. This is useful when designing the optical collection system since it provides information needed to determine the specifications of the lenses and CCD, as shown in what follows.

The Andor CCD camera has a CCD of 8.2mm square, which must fit wavelengths roughly from 532nm to 700nm, or most of the visible spectrum. If the CCD is too small, light from the experiment is lost and some species may not be observable. Conversely, if the light is dispersed very little, not using the majority of the CCD area, resolution will suffer and a large portion of the CCD will not be utilized. Therefore, it is desirable to design the optical system so that the light in the desired spectrum covers most of the CCD. Figure 20 shows light rays of different wavelength passing through the lens and focusing on the CCD.
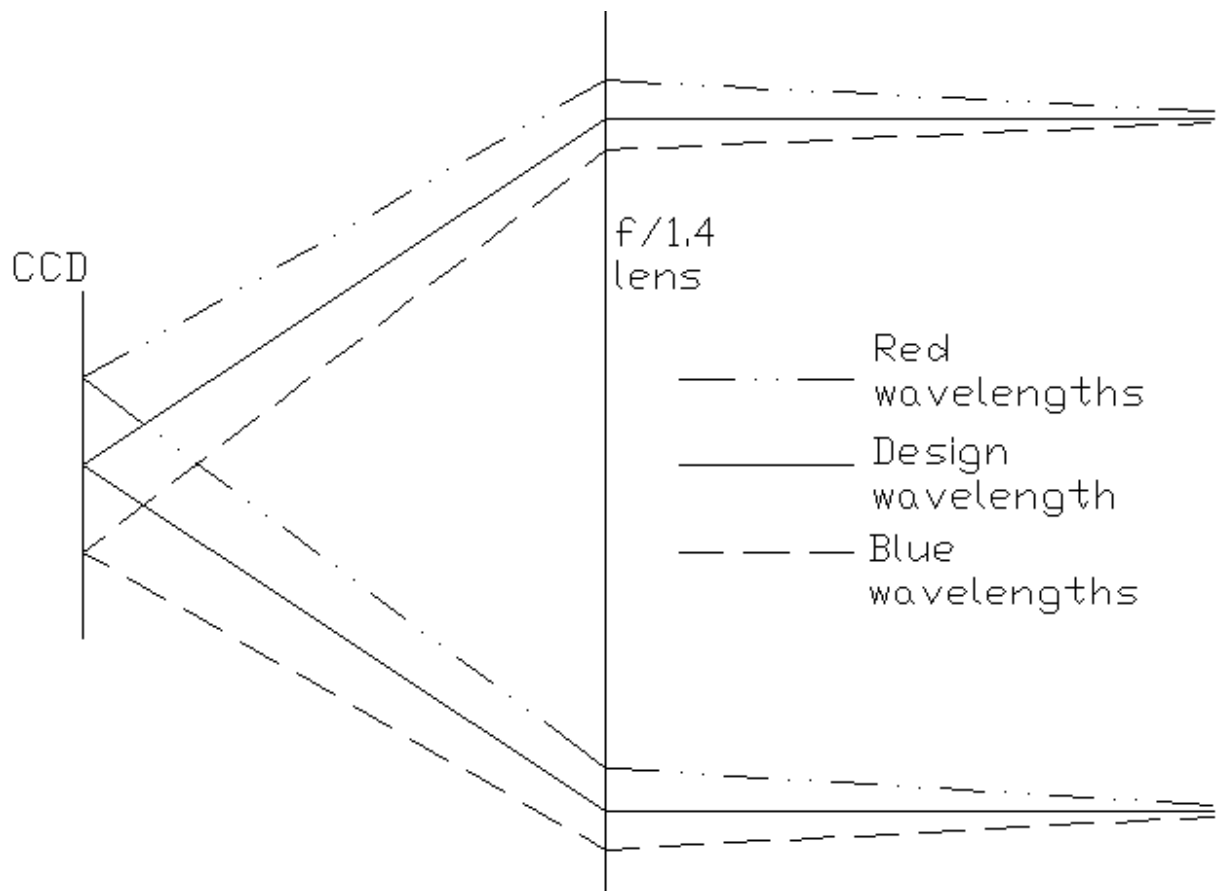
Fig. 20 Light Focusing on CCD

The diffraction grating has a design wavelength, which is the wavelength at which the

incident (θ_i) and diffracted (θ_d) angles are equal. The design wavelength for the Wasatch

Photonics 1269-03 transmissive grating is 600nm. The corresponding diffraction angle

is 21.1 degrees; the grating is mounted from vertical at this angle to maintain an angle of

incidence for the design wavelength (θ_i) at 21.1 degrees; the diffraction angle, θ_d, of the

design wavelength is equal to θ_i. Therefore, the red end of the spectrum (up to 700nm)

will propagate upwards from 600nm, and conversely the blue end (to 532nm) will be

below as shown in Fig. 21. At the CCD the shorter wavelengths will be recorded in the lower half of the CCD, 600nm will be located in the middle, and the longer wavelengths will appear at the top of the CCD. It is crucial to know the difference in height between the longest and shortest wavelengths in order to make sure that all desired wavelengths fit on the CCD.

In order to calculate the spread of the spectrum on the CCD ray tracing is used. After diffraction the collimated light passes through an f/1.4 lens and then a distance of 50mm (if thin lens approximations are used) through air before reaching the CCD. A ray impinges upon the lens at an angle θ and distance from the optical axis (beam radius) $\rho = 17.857$mm; the radius is taken to be the radius of the effective lens. Figure 21 below shows light being diffracted by the grating and impinging upon the lens. The lens is at an angle with respect to the horizontal equal to twice the diffraction angle of the design wavelength. This ensures that the design wavelength rays impinge upon the final focusing lens perpendicularly. The diffracted wavelength is measured with respect to the normal of the grating, therefore making the actual angle at which the light is diffracted with respect to horizontal equal to that wavelength's diffraction angle (θ_m) plus the design wavelength's diffraction angle. The total angle between horizontal and the design wavelength is twice the design wavelength's diffraction angle.
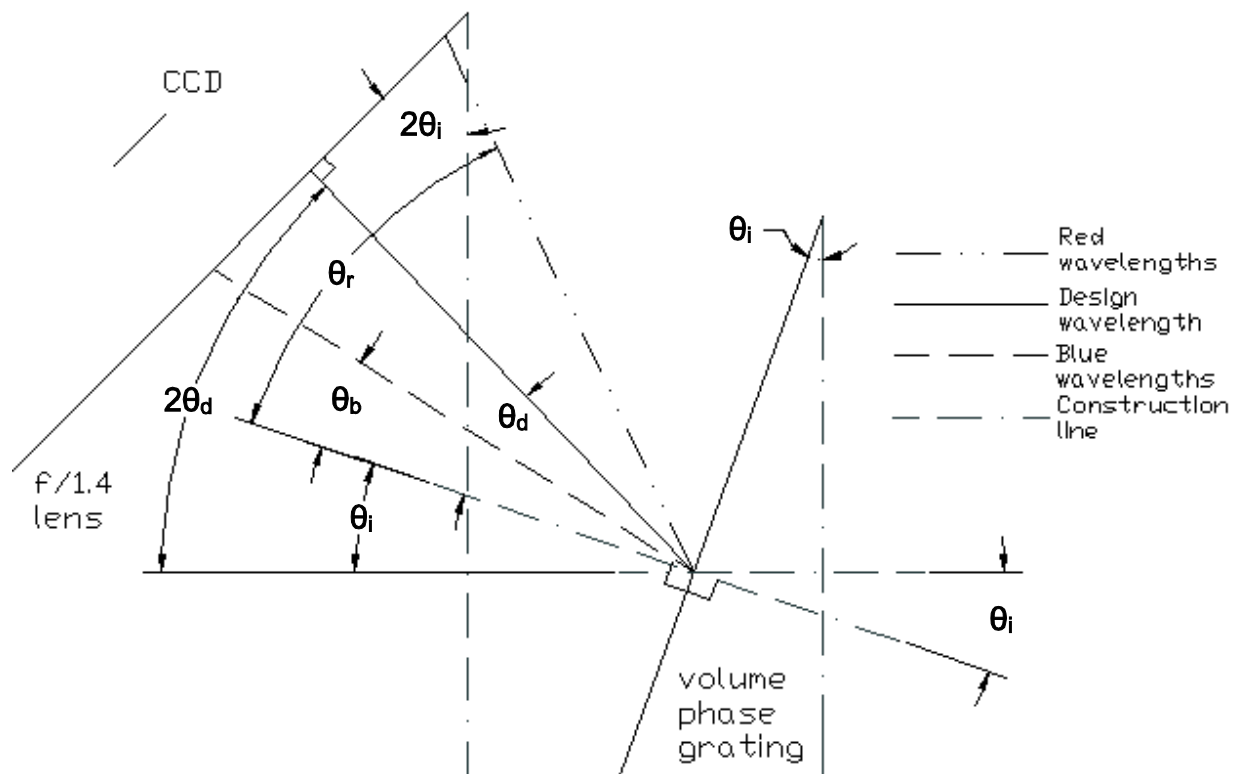
Fig. 21 Diffraction Grating Light Ray Geometry

For ray tracing subscripts are taken as 1 when impinging the lens and 2 when leaving, while subscript 3 is at the CCD. Equation (46) is the ray equation for the f/1.4 lens where f is the focal length of the lens (50mm in this case). Special care must be given to defining θ_1 since it defines angles both above and below the design wavelength; using the correct sign is paramount. For wavelengths equal or greater than 600nm $\theta_1 = \theta_r - \theta_i$, where θ_r is the diffraction angle for wavelengths at the red end of the spectrum (calculated from Equation (45)) and θ_i is the incident angle as shown in Fig. 21. This is because the diffraction angle is calculated relative to the line normal to the grating's surface as stated previously, which is θ_i. Similarly, for wavelengths less than 600nm θ_1

= -(θ_i − θ_b), where θ_b is the diffraction angle for wavelengths at the blue end of the spectrum in question (less than 600nm). This definition of θ_1 arises because blue light is diffracted less than the design wavelength. The diffraction angle of blue light is subtracted from the design wavelength diffraction angle. The negative sign is to indicate that the angle is measured from the design wavelength down (counterclockwise in Fig. 21).

$$\begin{bmatrix} \rho_2 \\ \theta_2 \end{bmatrix} = \begin{bmatrix} 1 & 0 \\ -1/f & 1 \end{bmatrix} \begin{bmatrix} \rho_1 \\ \theta_1 \end{bmatrix} \tag{46}$$

The light then passes through a distance d from the lens to the CCD, which is set equal to the lens's focal length (d = f). The ray tracing process is applied again using the appropriate ray matrix for light passing through a uniform medium over a distance as seen in Equation (47).

$$\begin{bmatrix} \rho_3 \\ \theta_3 \end{bmatrix} = \begin{bmatrix} 1 & d \\ 0 & 1 \end{bmatrix} \begin{bmatrix} \rho_2 \\ \theta_2 \end{bmatrix} \tag{47}$$

The radius ρ_3 is the distance from the center of the CCD to where each wavelength locates on the CCD in the vertical direction. Calculating this value over the wavelengths of the desired spectrum determines the vertical dimension of the CCD, or how much of the desired light is actually captured with a given CCD. As seen in the ray tracing

equations, ρ_3 is simply the radius of the effective lens plus the product of the focal length

with the sum of θ_2. Table 3 below shows the results using the 50mm f/1.4 Nikon lens.

Table 3   Spectrum height at CCD with 50mm lens

Wavelength [nm]	P_3 [mm]
700	6.619694
680	5.261731
660	3.922414
607	0.451317
600	0.000342
580	-1.27972
532	-4.30667
530	-4.43156
500	-6.29477

As seen in the table, only the design wavelength, nitrogen (607nm), oxygen

(580nm), and water (660nm) will be collected by the CCD.   In order to capture

wavelengths in the 532nm to 680nm (hydrogen) range a 35mm focal length final lens is

needed. Figure 22shows the vertical location on the CCD of the key wavelengths as a

function of lens focal length. Figures 26a through 31a in the Appendix show the same

data for a variety of other gratings.

Fig. 22 Wavelength Location at CCD as a Function of Focal Length
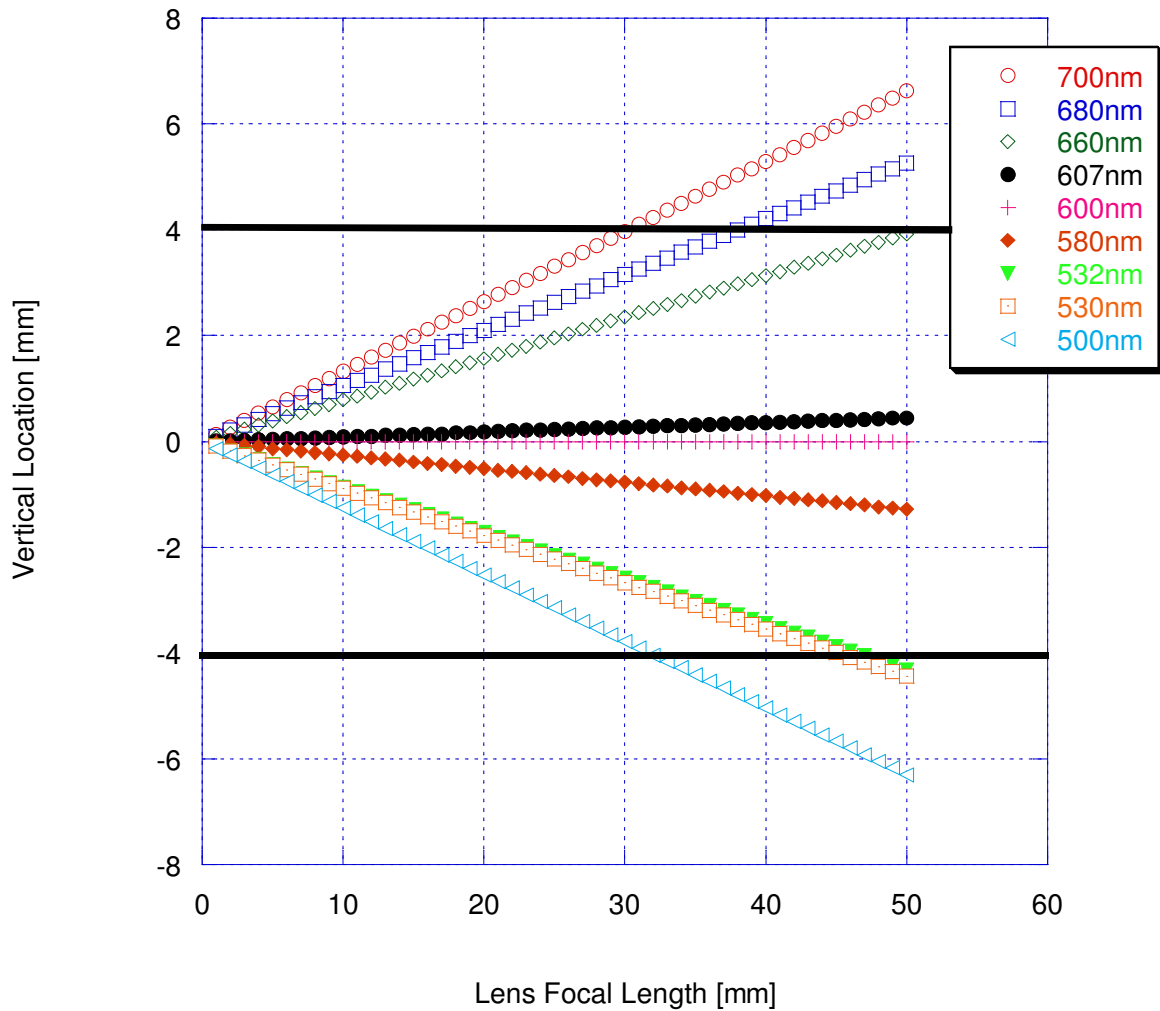
Since the CCD is 8.2mm in height, wavelengths appearing above 4.1mm and below -4.1mm will be lost. Figure 22 clearly shows the need for a 35mm lens to capture wavelengths of interest in flows. The light scattered by nitrogen and oxygen, 607nm and 580nm respectively, is easily captured using the 50mm lens, so the present system is adequate for experiments in air.

3.4.3.1 Grating Calibrations

The dispersion of a grating can be determined experimentally and the values contrasted to the theoretical design value. Using a white fiber-optic light source, band pass filters are placed in the optical system to permit only selected wavelengths. The wavelengths appear in different locations, which are noted, on the CCD. Then a comparison is made between the results of the diffraction calculations and the results of this test. This is the experimental verification of the CCD size calculations using ray tracing and the diffraction grating. It is used in practice to calibrate the system so that the data collected can be interpreted with relation to data previously attained.

A white, fiber optic light was chosen for this calibration, along with two band pass filters permitting 550nm and 600nm respectively. With the 550nm filter in place the vertical location of the light on the CCD is recorded as a certain pixel (i.e. pixel 231); in this case the vertical axis of the CCD is wavelength and the horizontal is distance along the probe volume. The 550nm filter is removed and in its place the 600nm filter is installed. Again, the vertical location of the light band is recorded. With this information linear relationship can be established between wavelength and pixels, and also wavelength and height on the CCD. This provides the dispersion of the diffraction grating used in this calibration. With this information, the ray tracing and diffraction calculations can be reversed so that the dispersion can be found for an unknown grating (from the grating equation).

Using the fiber optic light, 550nm and 600nm filters, a 512 x 512 EMCCD with 16μm pixels, and a diffraction grating from Wasatch Photonics the data shown for the "Lab" grating in Table 4 was produced.

Table 4   Dispersion of Wasatch diffraction gratings

Grating	Length on CCD [mm]	Dispersion [nm/mm]
Lab	3.248	15.394
1200lpmm @ 600nm	12.914	15.487
1800lpmm @ 532nm	23.093	8.660
600lpmm @ 600nm	6.103	32.767
1200lpmm @ 785nm	12.429	16.092
1200lpmm @ 830nm	29.575	6.762
1200lpmm @ 550nm	13.086	15.283

As seen in the table, the 1200lpmm @ 600nm grating most closely matches the one used in the lab. The length on the CCD is different for the Lab grating and the 1200lpmm @ 600nm because the Lab grating value was measured for the 50nm wavelength band used in the calibration while the 1200lpmm @ 600nm grating value uses a 200nm wavelength band corresponding to the approximate wavelength range on interest. Data for the Lab grating was found experimentally as described above, while the others were calculated by the grating equation and ray tracing. This was done to determine the properties of the grating being used in the lab and investigate the effects of other gratings and their usefulness in this research.

For the calculated gratings (all other than "Lab"), the wavelength range used was 500nm to 700nm, for a difference of 200nm. This range encompasses the Stokes Raman shifts of combustion products with laser excitation at 532nm. Table 5 contains the upper

and lower wavelength limits for the respective gratings and the difference between them. These values were used to generate the data in Table 4. The grating designations are given in the groove frequency at a design wavelength. For example a grating with groove frequency of 1200lpmm at design wavelength of 500nm would read "1200@500".

Table 5   Wavelength range calculated for Wasatch gratings

Grating Property	1200@600	1800@532	600@600	1200@785	1200@830	1200@550
Bottom	-6.295	-3.214	-3.035	-18.055	-20.960	-3.200
Top	6.620	19.880	3.069	-5.626	-8.616	9.887
Range	12.914	23.094	6.104	12.429	12.343	13.086

The "bottom" values are the lowest vertical location, in mm on the CCD, of light captured (the 500nm light). Similarly, the "top" values correspond to CCD locations of the 700nm light rays (again in mm). The "range" values are the difference between the top and bottom values. These calculated values were used to generate theoretical calibration curves for the gratings as described below.

Figure 23 shows the calibration curve with a trend line extrapolated to determine the viewable wavelength range.
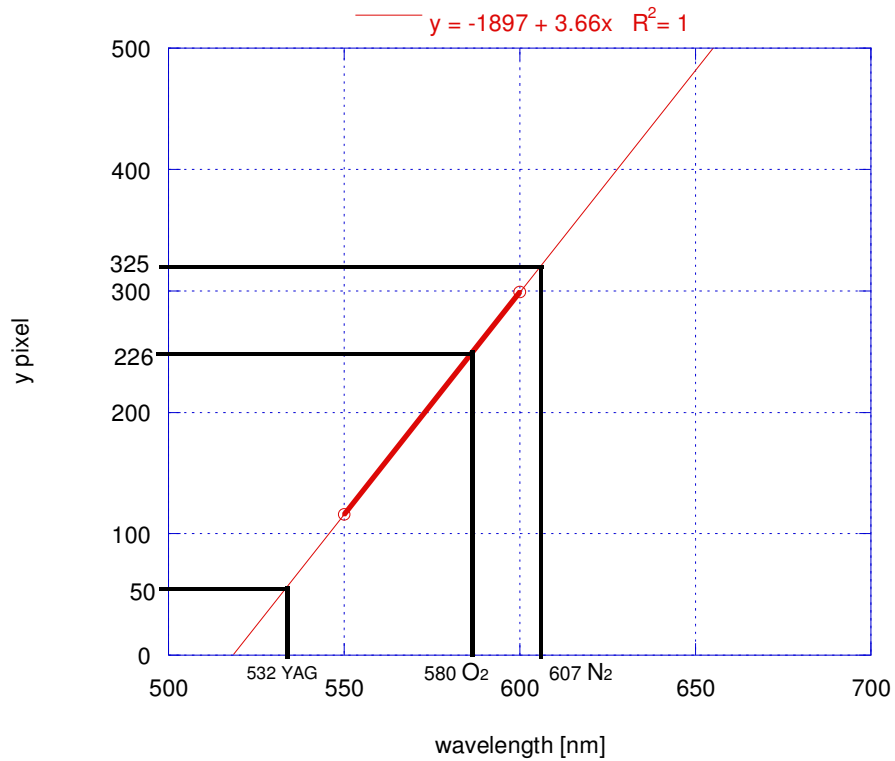
Fig. 23 Calibration Graph for Lab Grating as of 11/29/07

As can be determined from the calibration equation (top of graph), this grating and optical system capture wavelengths from 518nm to 658nm, which will capture the Stokes Raman shifts of nitrogen (607nm) and oxygen (580nm). These wavelengths, along with the incident laser are marked with their corresponding pixel in the figure. The laser, oxygen, and nitrogen are located at pixel 50, 226, and 325 respectively. Table 6 presents the theoretical calibration data for the gratings.

Table 6   Pixel locations

Wavelength [nm]	1200@600	1800@532	600l@600	1200@785	1200@830	1200@550
500	-137.42	55.135	66.297	-872.40	-1054.0	56.032
700	669.73	1498.5	447.78	-95.617	-282.50	873.93

Negative values indicate the light ray lands at a point below the centerline of the grating. Counting from zero at the bottom of the CCD means values below zero and above 512 pixels are not on the CCD, so the light at those locations will not be captured. As seen in the table, the 600lpmm@600nm grating is the only one to capture the entire range, while the 1200lpmm@600nm grating captures much of it. Table 7 displays the wavelength range captured with each grating using the 50mm lens.

Table 7   Wavelength range captured

Wavelength [nm]	1200@600	1800@532	600l@600	1200@785	1200@830	1200@550
Min	534.05	492.36	465.26	724.63	768.05	486.29
Max	660.91	536.31	733.68	856.49	900.79	612.49

As seen in the table, the 1200lpmm@600nm grating captures most of the desired wavelengths and the 600lpmm@600nm grating captured a larger range than necessary. The 1800lpmm@532nm grating would be useful for anti-Stokes measurements since it captures wavelengths in the range of blue-shifted light at 532nm excitation.   The 1200lpmm@785nm and 1200lpmm@830nm are too far infrared for the Stokes Raman

transitions of air. The 1200lpmm@550nm grating captures light scattered by air, but the Stokes nitrogen light, at 607nm, would be very close to the upper edge of the CCD. Figure 24 shows the theoretical calibration lines and equations for the gratings with the position of the laser and Stokes lines for nitrogen and oxygen shown.
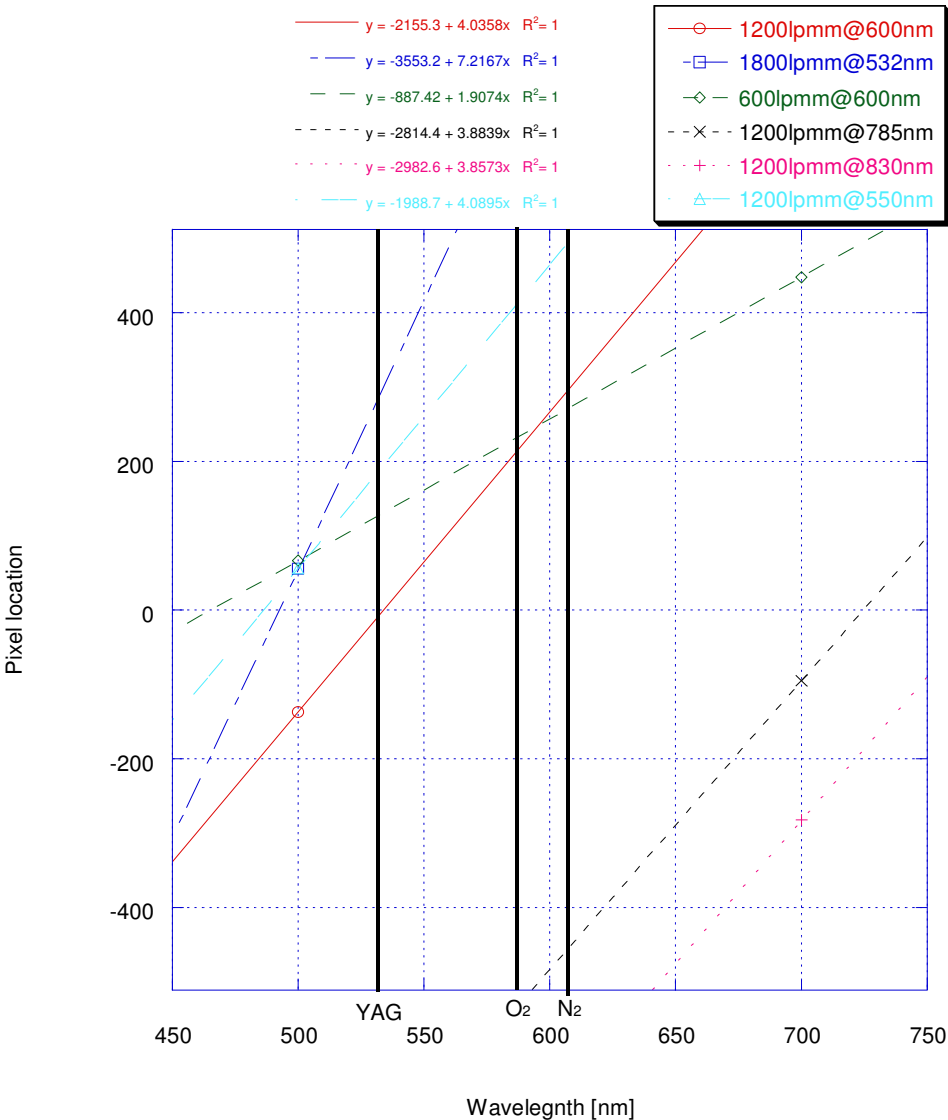

Fig. 24 Theoretic Calibration Graph

The slope of the calibration line represents the dispersion of the grating, and it is clear that the 1800lpmm grating has the steepest slope while the 600lpmm has the flattest; the figure also shows the information from Table 6 graphically. In the case where the light is spread too much to fit the desired wavelength on the CCD a lens with a shorter focal length should be used. Also, the optical system is designed to capture visible light in the 500nm to 700nm range. Many of these gratings have design wavelengths that are outside of this range. This causes the spread of light right to be asymmetrical with respect to the midpoint of the wavelength range being examined (600nm) with much of the light directed above or below the CCD. This may cause light rays to not be captured even if the range covers less than 512 pixels in size (as in the 1200lpmm@550nm grating). Figures 26a through 31a of the Appendix show the locations (in millimeters) of desired wavelengths as a function of CCD camera lens focal length for several gratings; the data was generated via the grating equation and ray tracing. This is a graphical representation of how the wavelengths map to the CCD in both spectral width and location. The asymmetrical collection is easily seen.

3.4.4   Camera

The camera for this spectrometer is the Andor Technologies iXon[EM] + 897 16-bit back illuminated EMCCD. It was selected for its high quantum efficiency, low dark current, and hardware binning capabilities. With thermoelectric and water cooling down to -100C, minimizing dark current, the quantum efficiency can reach over 90%. Figure 25, from the camera manufacturer[25], shows the quantum efficiency of the CCD camera.

It is seen than within the desired wavelength range that the quantum efficiency reaches

approximately 97% with the visible anti-reflection coating (BV).
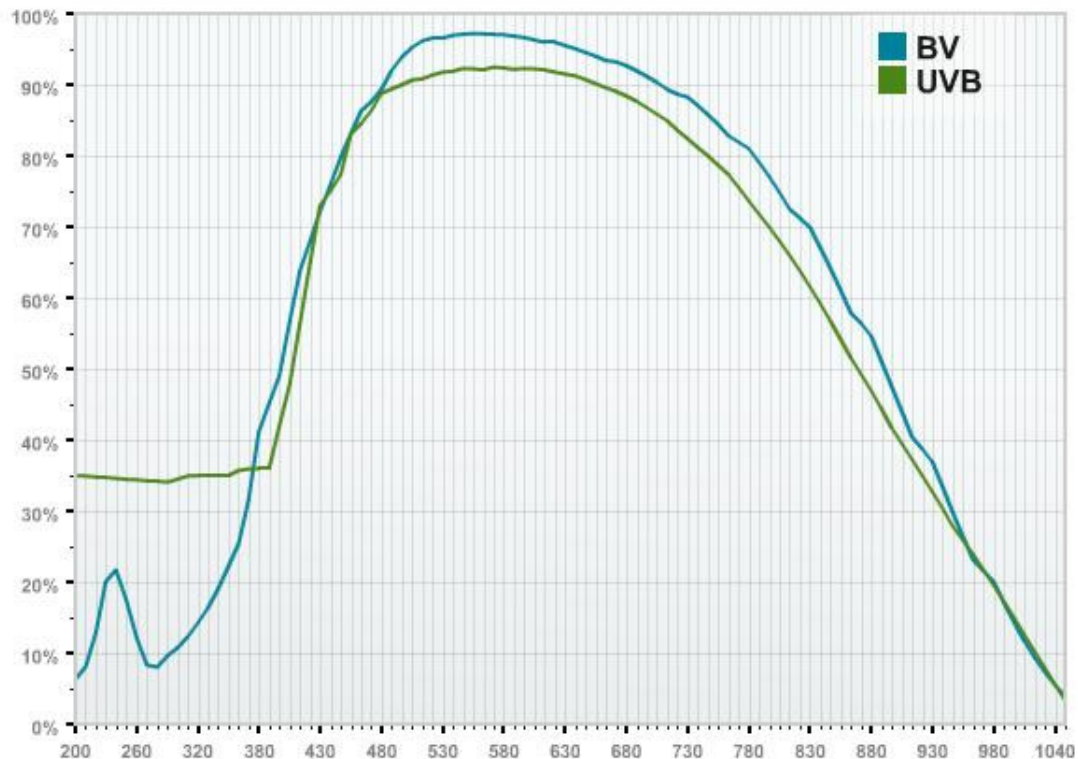
BV - Back Illuminated - Visible Anti Reflection Coating - 550nm

UVB - Back Illuminated with UV Phosphor

Fig. 25 Quantum Efficiency Plot for CCD Camera

This is a very high quantum efficiency which is an integral part of the system since the

signal levels are so low. Having over 90 photoelectrons for every 100 photons collected

helps provide the strongest signal possible.

The CCD is an E2V frame transfer type of 512x512 pixels (16μm length) for an

overall size of 8.2mmx8.2mm. The CCD has a frame transfer rate of 35 frames per

second and a maximum readout rate of 10MHz. The camera is capable of hardware

superpixel binning in standard configurations such as 4x4 or custom bins. Hardware superpixel binning increases the signal-to-noise ratio (S/N). Binning the signal of several pixels to create a superpixel increases the signal strength while the readout noise of the camera remains the same. For this reason hardware binning is a crucial feature of the camera. It is possible to do superpixel binning in software, however, the noise of the camera is added along with the captured signal.

3.5 Photon Count

The intensity of Raman and Rayleigh signals depends on the number of photons collected for each wavelength and is paramount for measuring temperature and density using light scattering techniques. The photon count depends on many factors including laser power and beam dimensions, state of the gas, optical system, and the scattering species.

The total number density (N), or molecules present per unit probe volume, is of particular importance since the energy scattered is directly proportional. Using Avogadro's constant and the fact that a mole of gas occupies 22.4 liters at standard temperature and pressure, Equation (48) is used to calculate N_o (Loschmidt number). This applies only to ideal gases, an assumption which holds for the flowfields being studied in this laboratory. The Loschmidt number is 2.687×10^{25} molecules per cubic meter (at STP).

$$N_o = \frac{A_v}{22.4L} \tag{48}$$

The key component of the collection optics is the Nikkor f/1.8 85mm lens. Again, the scattered light is proportional to the solid angle, therefore increase the solid angle will increase the collected signal.

The scattered energy is also proportional to the scattering cross section in addition to the solid angle. The scattering cross section is the ratio of radiant energy flux per unit solid angle. Each species has a different Raman cross section, many of which have been determined experimentally, with nitrogen's being $0.37 \times 10^{-30} cm^2/sr$[13]. This value is for the Q-branch vibrational component (at 532nm incident wavelength) which is predominant in rotational-vibrational Raman scattering.

With the above information the scattered energy can be calculated by Equation (49) [13]:

$$E_{sv} = E_o N_{N2} \Omega L \varepsilon \left(\frac{\partial \sigma}{\partial \Omega} \right)_{vib} \tag{49}$$

where E_{sv} is the scattered vibrational energy, E_o is the incident energy (0.8J), $\partial \sigma_v / \partial \Omega$ is the differential vibrational scattering cross section, and ε is the optical system efficiency factor (taken to be 1 initially, must be determined experimentally). N_{N2} is the number density for the desired species (nitrogen in this example) and is equal to the mole fraction of nitrogen in air multiplied by the total number density. Substituting the values

into Equation (49) shows the scattered energy to be 2.305×10^{-15} J with taking L to be one pixel. To find the number of photons collected per pixel (PH) all that is necessary is to divide this energy by the energy of one Stokes photon (E_{ph}) at 607nm wavelength (λ) as shown in Equations (50) and (51).

$$E_{ph} = h\upsilon = \frac{hc}{\lambda} \tag{50}$$

$$PH = \frac{E_{sv}}{E_{ph}} \tag{51}$$

The energy of one photon is easily found by multiplying Plank's constant (h) by the frequency υ, where υ is equal to the speed of light (c) divided by the wavelength (λ). For 607nm wavelength the energy of one photon is 3.27×10^{-19} J. Dividing the scattered energy by the energy of one photon reveals that 7,043 photons are collected by each superpixel.

The calculations were repeated for oxygen substituting the appropriate values. The result is scattered energy of 7.783×10^{-16}J. With a Stokes wavelength of 580nm, the collected photons scattered by oxygen was found to be 2,272 per superpixel.

To find the number of photons scattered due to rotational Raman the same calculations were followed using the rotational cross section in place of the vibrational cross section. The rotational scattering cross sections in Eckbreth were given for excitation at 488nm. To obtain the appropriate rotational cross sections the rotational

cross section for 488nm excitation was scaled based on the principle that scattering is proportional to the forth power of frequency. The rotational cross sections were found to be $3.65 \times 10^{-30} cm^2/sr$ for nitrogen and $12.64 \times 10^{-30} cm^2/sr$ for oxygen. The corresponding photon counts were found to be 69,480 for nitrogen and 61,110 for oxygen. Even though these photons are contributed by all rotational levels (J values) as shown in Fig. 2 and Fig. 3, their high numbers offer the possibility for a temperature determination through the rotational Raman measurement.

A similar calculation is followed to find the number of photons collected through Rayleigh scattering. The main difference between Rayleigh and Raman scattering is the scattering cross section. The total Rayleigh scattering cross section is defined by Equation (52)[10].

$$\sigma_{ray} = \frac{4\pi^2(n-1)^2}{\lambda^4 N_o{}^2} \tag{52}$$

In Equation (52) n is the index of refraction for the given species at standard temperature and pressure, λ is the wavelength of the laser, and N_o is the Loschmidt number which is equal to 2.687×10^{19} cm^{-3}, as shown previously. For ideal gases, the Loschmidt number is the molecular density of the gas at standard temperature and pressure[10]. The value σ_{ray} corresponds to an integral cross section and it accounts for the photons scattered over an entire sphere of 4π steradians. To convert this to the

differential scattering cross section used in Equation (49) it is necessary to divide the

value of σ_{ray} by 4π steradians, resulting in Equation (53).

$$\left(\frac{\partial\sigma}{\partial\Omega}\right)_{ray} = \frac{\pi(n-1)^2}{\lambda^4 N_o{}^2} \tag{53}$$

With the differential Rayleigh scattering cross section determined, the photon count is

calculated following the same method used for the Raman case. The two differences are

the scattering cross section, as mentioned, and the energy of one photon. In Equation

(50), λ for Rayleigh scattering is the excitation wavelength (532nm) rather than the

Stokes shifted wavelength used for Raman. Taking the species concentrations for air

into account (approximately 79% nitrogen and 21% oxygen), the number of photons

scattered for nitrogen and oxygen was calculated to be 8.048×10^5 and 1.769×10^5,

respectively.

Forming the ratio of Rayleigh scattering to total Raman scattering (pure

rotational and rotational-vibrational) it is found that Rayleigh scattered photons

numbered 139.387 and 432.086 times greater than the rotational-vibrational Raman

scattered photons of nitrogen and oxygen, respectively. The Rayleigh to pure rotational

Raman was 7.517. Rotated at 10 degrees, the Semrock filter permits only 0.012440% of

the light at 532nm. The total Rayleigh scattering count is 9.817×10^5 photons, therefore

only 122 Rayleigh photons will reach the CCD, which is sufficiently low as to avoid

significant interference with pure rotational Raman scattering.

4. SUMMARY

4.1   General

This work has described the design and construction of a combined rotational-vibration Raman spectroscopy system utilizing a newly developed transmissive grating spectrometer. This system has the ability to collect rotational and rotational-vibrational Raman scattering on one CCD by blocking the Rayleigh scattering with a long-pass filter. A method for measuring mixture temperature from the decay of the pure rotational profiles has been presented. Using the temperature, the partial pressures were derived from the rotational-vibrational spectrum through the equation of state. Thus far the system has been used to capture the spectra in ambient air conditions, demonstrating the overall soundness of the system's design and setup.

4.2   Future Work

Future work with this system in the short term involves measuring temperature and pressure in air jets using the analysis methods that were broadly outlined in the present work. Performing experiments with high-speed flames, such as methane-air flames issuing from underexpanded jet nozzles, will follow. Line imaging will allow for the calibration of differences between measured quantities and ultimately the calculation of scalar dissipation rates in supersonic flows under nonisobaric conditions[11].

REFERENCES

[1]Peters, N., *Turbulent Combustion.* Cambridge University Press, Cambridge, 2000.

[2]Ben-Yakar, A. and Hanson, R.K., "Cavity Flame-Holders for Ignition and Flame Stability in Scramjets: An Overview," *Journal of Propulsion and Power,* Vol. 17, No. 4, 2001, pp. 869-877.

[3]McClinton, C.R., Rausch, V.L., Nguyen, L.T. and Stiz, J.R., "Preliminary X-43 Flight Test Results," *Acta Astronautica,* Vol. 57, No. 2-8, 2005, pp. 266-276.

[4]Anderson, J.D., *Fundamentals of Aerodynamics.* McGraw-Hill, New York, 2001.

[5]Farrow, R.L., Mattern, P.L. and Rahn, L.A., "Comparison Between CARS and Corrected Thermocouple Temperature in a Diffusion Flame," *Applied Optics,* Vol. 21, No. 17, 1982, pp. 3119-3125.

[6]Lederman, S., Bloom, M.H., Bornstein, J. and Khosla, P.K., "Temperature and Specie Concentration Measurements in Flow Fields," *International Journal of Heat and Mass Transfer,* Vol. 17, 1974, pp. 1479-1486.

[7]Eckbreth, A.C., Bonczyk, P.A. and Verdieck, J.F., "Combustion Diagnostics by Laser Raman and Fluorescence Techniques," *Progress in Energy and Combustion Science,* Vol. 5, No. 4, 1979, pp. 253-322.

[8]Masri, A.R., Dibble, R.W. and Barlow, R.S., "The Structure of Turbulent Nonpremixed Flames Revealed by Raman-Rayleigh-LIF Measurements," *Progress in Energy and Combustion Science,* Vol. 22, No. 4, 1996, pp. 307-362.

[9]Cabra, R., Chen, J.-Y., Dibble, R.W., Karpetis, A.N. and Barlow, R.S., "Lifted Methane-air Jet Flames in a Vitiated Coflow," *Combustion and Flame,* Vol. 143, 2005, pp. 491-506.

[10]Zhao, F.-Q. and Hiroyasu, H., "The Applications of Laser Rayleigh Scattering to Combustion Diagnostics," *Progress in Energy and Combustion Science,* Vol. 19, 1993, pp. 447-485.

[11]Karpetis, A.N. and Barlow, R.S., "Measurements of Flame Orientation and Scalar Dissipation in Turbulent Partially Premixed Methane Flames," *Proceedings of the Combustion Institute,* Vol. 30, 2005, pp. 665-672.

[12]Karpetis, A.N., Settersten, T.B., Schefer, R.W. and Barlow, R.S., "Laser Imaging System for Determination of Three-dimensional Scalar Gradients in Turbulent Flames," *Optics Letters,* Vol. 29, No. 4, 2004, pp. 355-357.

[13]Eckbreth, A.C., *Laser Diagnostics for Combustion Temperature and Species.* Taylor and Francis, New York, 1996.

[14]Werhmeyer, J.A., Yeralan, S. and Tecu, K.S., "Linewise Raman-Stokes/anti-Stokes Temperature Measurements in Flames Using an Unintensified Charge-coupled Device," *Applied Physics B: Lasers & Optics,* Vol. 62, No. 1, 1996, pp. 21-27.

[15]Lederman, S., "The Use of Laser Raman Diagnostics in Flow Fields and Combustion," *Progress in Energy and Combustion Science,* Vol. 3, No. 1-A, 1977, pp. 1-34.

[16]Van Vleck, J.H., "On sigma-Type Doubling and Electron Spin in the Spectra of Diatomic Molecules," *Physical Review,* Vol. 33, No. 4, 1929, pp. 467-506.

[17]Kojima, J. and Nguyen, Q.-V., "Quantitative Analysis of Spectral Interference of Spontaneous Raman Scattering in High-pressure Fuel-rich H_2-Air Combustion," *Journal of Quantitative Spectroscopy and Radiative Transer,* Vol. 94, No. 3-4, 2005, pp. 439-446.

[18]Kojima, J. and Nguyen, Q.-V., "Measurement and Simulation of Spontaneous Raman Scattering in High-pressure Fuel-rich H_2-Air Flames," *Measurement Science and Technology,* Vol. 15, No. 3, 2004, pp. 565-580.

[19]Hill, P.G. and Peterson, C.R., *Mechanics and Thermodynamics of Propulsion.* Addison Wesley Longman, Reading, MA, 1992.

[20]Tipler, P.A., *Physics for Scientists and Engineers: Electricity and Magnetism, Light.* Worth Publishers Inc., New York, 1999.

[21]Fowles, G.R., *Introduction to Modern Optics.* Dover, New York, 1989.

[22]Semrock Inc., "Technical Information: Edge Filter Spectra vs. Angle of Incidence," http://www.semrock.com/TechNotes/TN_Raman_SpectrumvsAOI.htm, 2008.

[23]Hutley, M.C., *Diffraction Gratings.* Academic Press, Oxford, 1982.

[24]Arns, J.A., Colburn, W.S. and Barden, S.C., "Volume Phase Gratings for Spectroscopy, Ultrafast Laser Compressors, and Wavelength Division Multiplexing," *Current Developments in Optical Design and Optical Engineering VIII,* SPIE, Vol. 3779, 1999, pp. 313-323.

[25]Andor Technology, "iXon^{EM} + 897 QE Curves,"
http://www.andor.com/scientific_cameras/ixon/models/default.aspx?iProductCodeID=3&tab=tabQECurves, 2008.
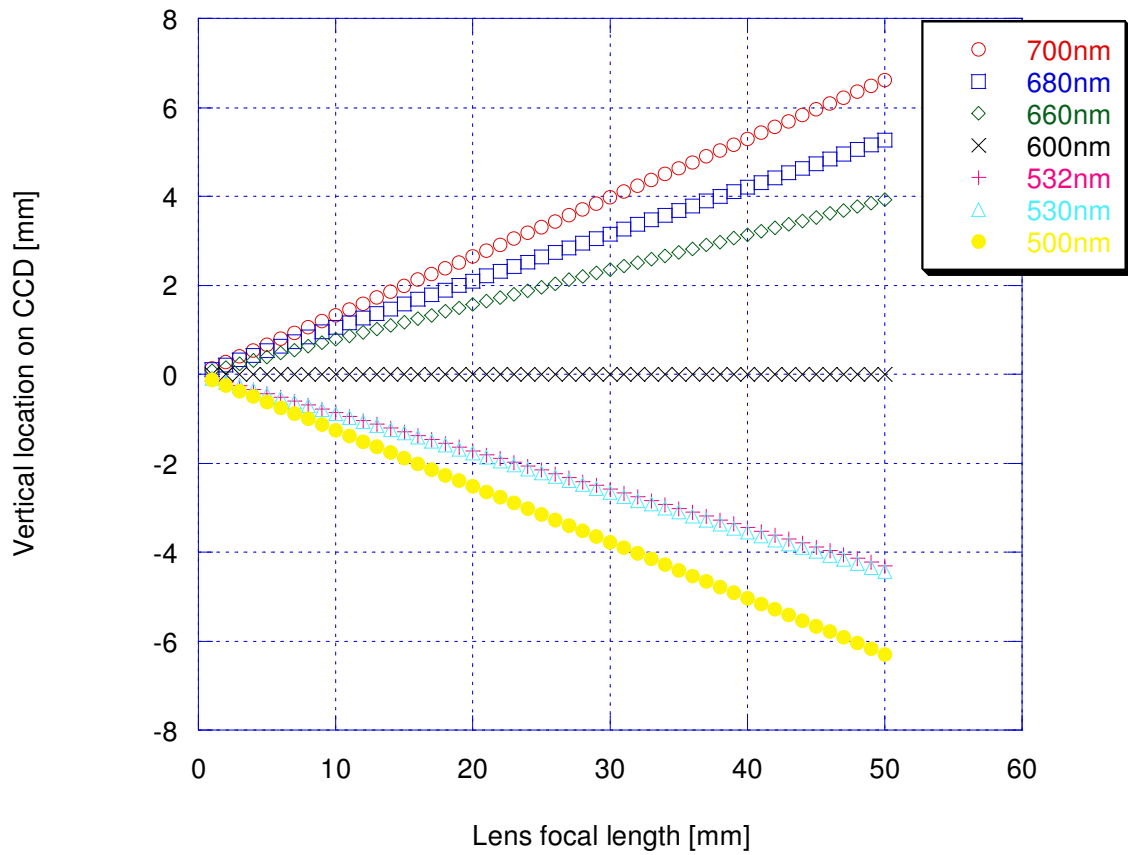
APPENDIX

Fig. 26a Wavelength Location at CCD as a Function of Focal Length for 1200lpmm@600nm Grating
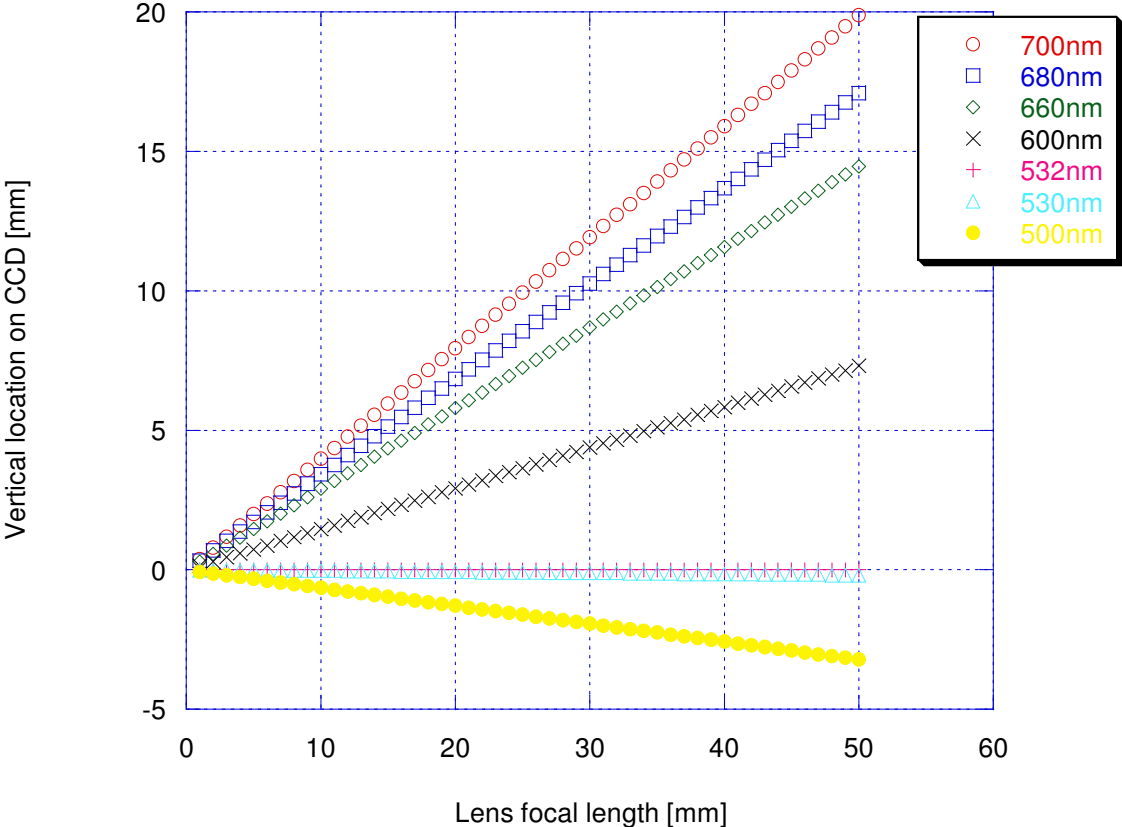
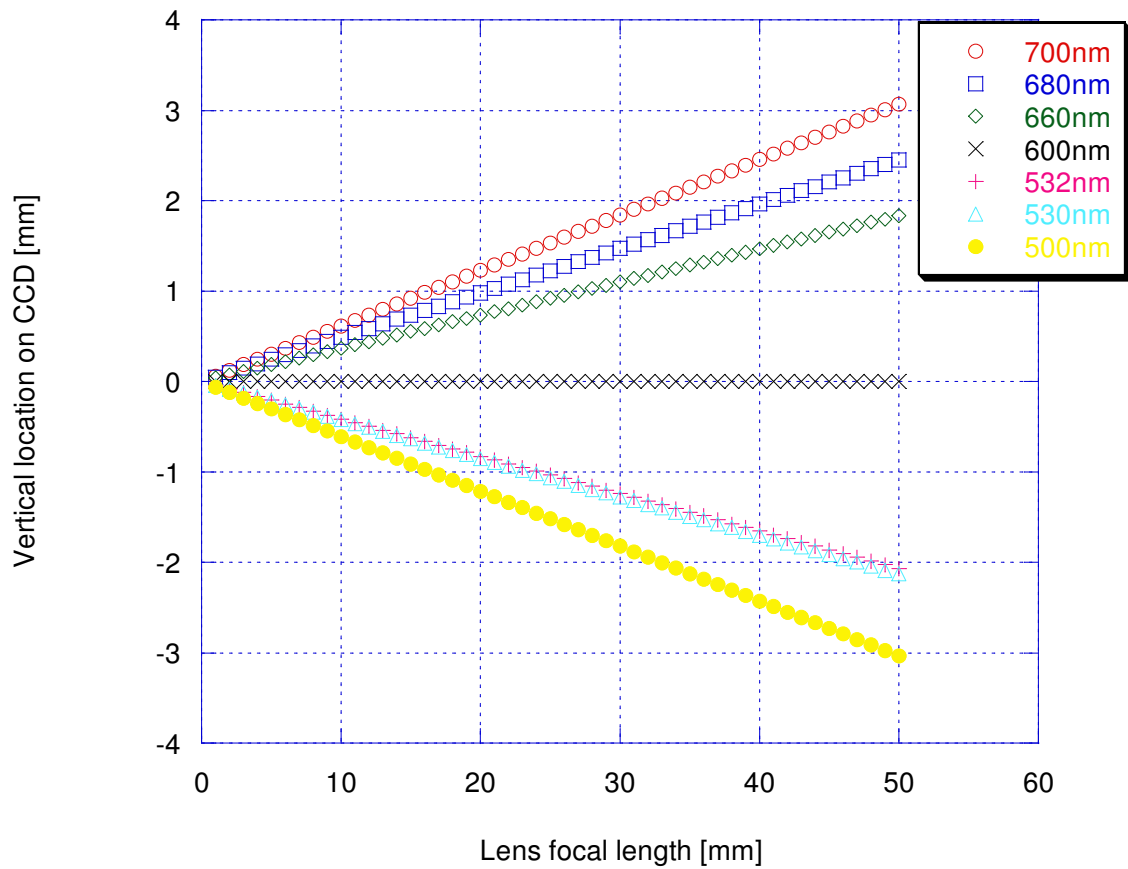**Fig. 27a Wavelength Location at CCD as a Function of Focal Length for 1800lpmm@532nm Grating**

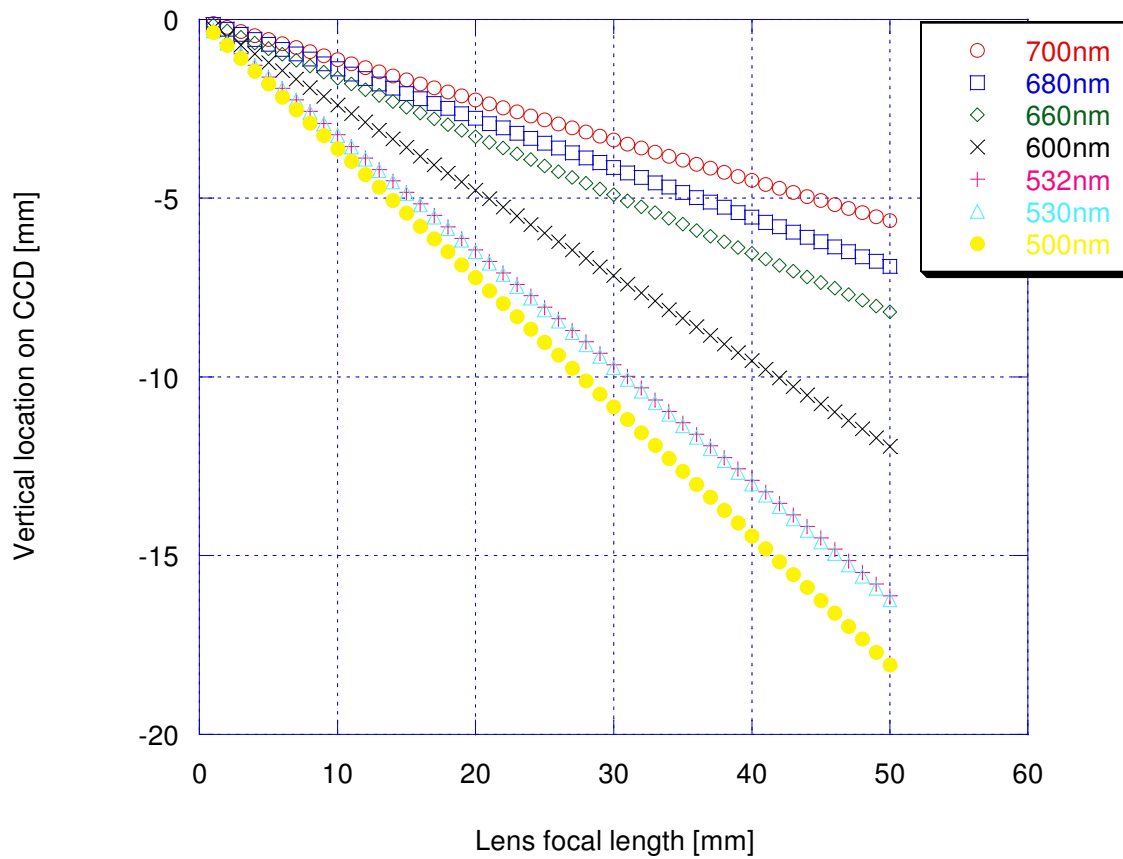**Fig. 28a Wavelength Location at CCD as a Function of Focal Length for 600lpmm@600nm Grating**

Fig. 29a Wavelength Location at CCD as a Function of Focal Length for 1200lpmm@785nm Grating
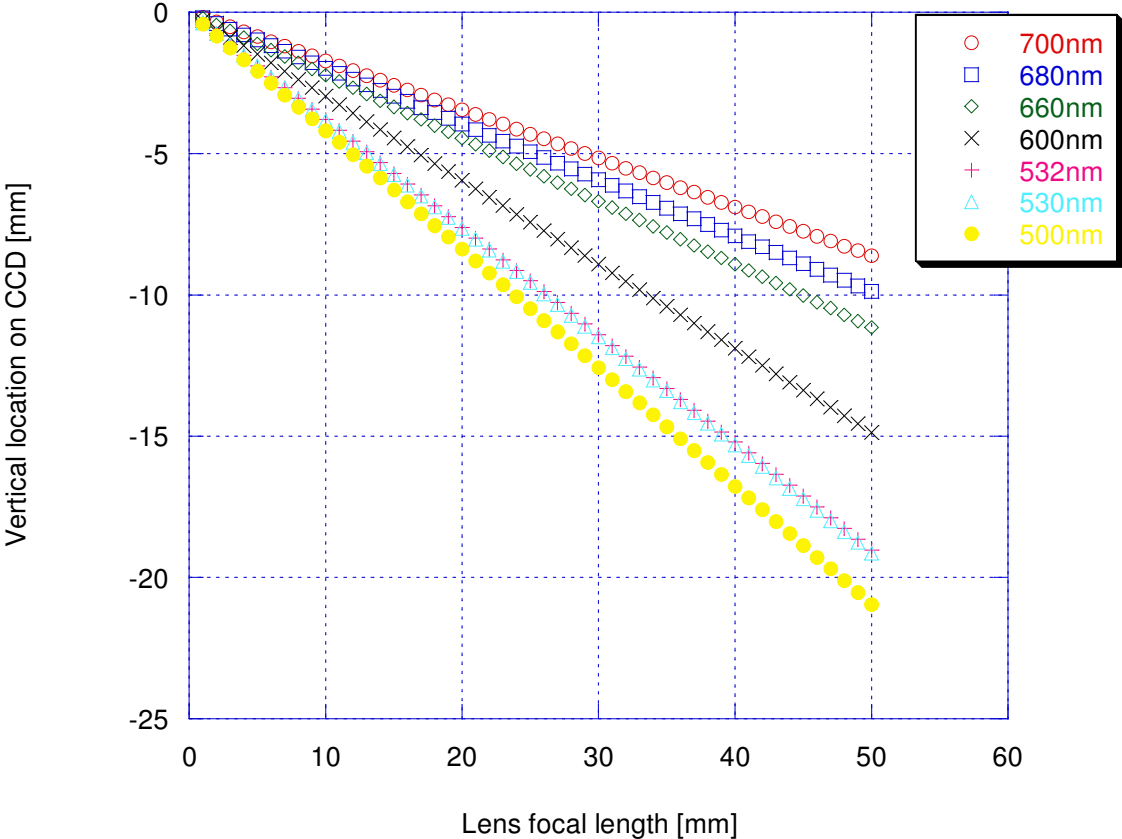
Fig. 30a Wavelength Location at CCD as a Function of Focal Length for 1200lpmm@830nm Grating
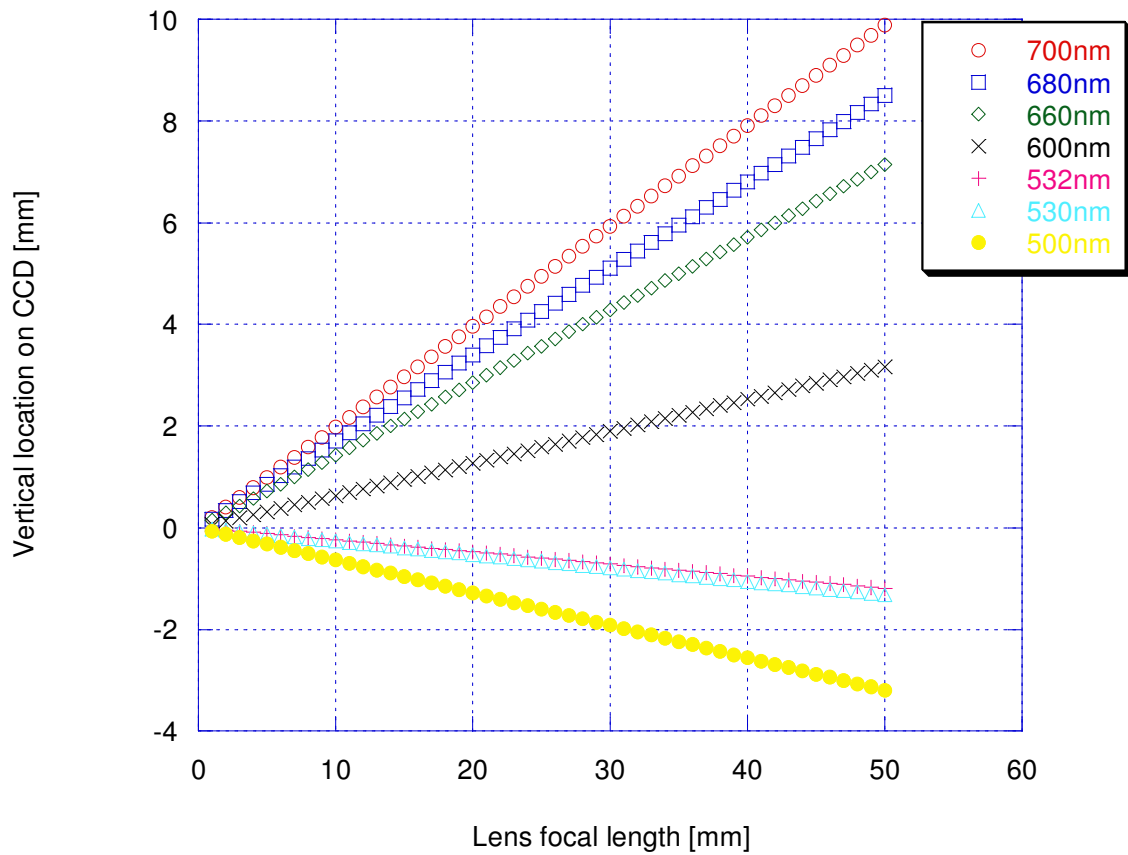
Fig. 31a Wavelength Location at CCD as a Function of Focal Length for 1200lpmm@550nm Grating

VITA

Name: Benjamin Nathan Cohen

Address: Department of Aerospace Engineering
H.R. Bright Building Rm. 701 Ross St. - TAMU 3141
College Station, TX 77843-3141

Email Address: bnc2593@aero.tamu.edu

Education: B.S. with Distinction, Aerospace Engineering, University of
Oklahoma, 2006

M.S., Aerospace Engineering, Texas A&M University, 2008